

Mutual neutralisation reactions in atmospheric and industrial plasmas

Mathias Poline

November 18, 2022



Licentiate thesis
Stockholm University
Department of Physics

Contents

1	Introduction	6
1.1	Historical overview	6
1.2	MN in planetary atmospheres	10
1.3	MN in industrial and applied plasmas	11
2	Experimental apparatus	13
2.1	Ion production	13
2.2	The ion storage rings	14
2.3	Detection system	15
3	Data Analysis	17
3.1	Preliminary data evaluation	17
3.2	Two particle imaging	18
3.3	Two particle simulations	19
3.4	Three particle imaging	23
3.5	Three particle simulation	23
3.6	Branching ratios	24
3.7	Break-up dynamics	27
4	Theoretical calculations	29
4.1	Landau-Zener model	29
4.2	Asymptotic centered anion model	30
4.3	Multiconfigurational calculations	31
4.4	Ab initio calculations	31
5	Results	33
5.1	Paper I: Mutual neutralisation of O^+ with O^+	33
5.2	Paper II: Mutual neutralisation of N^+ with O^-	35
5.3	Paper III: Mutual neutralisation of I^+ with I^-	37
5.4	Preliminary results: Mutual neutralisation of O_2^+ with O^-	39
6	Conclusions and Outlook	41

List of Papers

The following papers, referred to in the text by their Roman numerals, are included in this thesis.

PAPER I: Mutual neutralisation of O⁺ with O⁻: investigation of the role of metastable ions in a combined experimental and theoretical study

Mathias Poline, Arnaud Dochain, Stefan Rosén, Jon Grumer, MingChao Ji, Gustav Eklund, Ansgar Simonsson, Peter Reinhed, Mikael Blom, Nicholas S. Shuman, Shaun G. Ard, Albert A. Viggiano, Mats Larsson, Henrik Cederquist, Henning T. Schmidt, Henning Zettergren, Xavier Urbain, Paul S. Barklem, Richard D. Thomas. *Phys. Chem. Chem. Phys.*, **23**, 24607-24616 (2021)
DOI: 10.1039/D1CP03977F

PAPER II: Storage ring study of the mutual neutralisation of N⁺ with O⁻

Mathias Poline, Arnaud Dochain, Stefan Rosén, Jon Grumer, MingChao Ji, Ansgar Simonsson, Peter Reinhed, Nicholas S. Shuman, Shaun G. Ard, Albert A. Viggiano, Mats Larsson, Henning T. Schmidt, Xavier Urbain, Paul S. Barklem, Richard D. Thomas. *Phys. Rev. A*, **105**, 062825 (2022)
DOI: 10.1103/PhysRevA.105.062825

PAPER III: Final-state-resolved mutual neutralization in I⁺-I⁻ collisions

Mathias Poline, Xiang Yuan, Sylvain Badin, MingChao Ji, Stefan Rosén, Suvasthika Indrajith, Richard D. Thomas, Henning T. Schmidt, Henning Zettergren, Andre Severo Pereira Gomes, and Nicolas Sisourat. *Phys. Rev. A*, **106**, 012812 (2022)
DOI: 10.1103/PhysRevA.106.012812

The following papers are not included in this thesis.

PAPER IV: Theoretical studies of infrared signatures of proton-bound amino acid dimers with homochiral and heterochiral moieties

Mathias Poline, Oleksii Rebrov, Mats Larsson, Vitali Zhaunerchyk. *Chirality*, **32**, 359-369 (2020)
DOI: 10.1002/chir.23165

PAPER V: Structure of Proton-Bound Methionine and Tryptophan Dimers in the Gas Phase Investigated with IRMPD Spectroscopy and Quantum Chemical Calculations

Åke Andersson, Mathias Poline, Meena Kodambattil, Oleksii Rebrov, Estelle Loire, Philippe Maître, and Vitali Zhaunerchyk. *J. Phys. Chem. A*, **124**, 12 2408–2415 (2021)
DOI: 10.1021/acs.jpca.9b11811

PAPER VI: IRMPD Spectroscopy of Homo- and Heterochiral Asparagine Proton-Bound Dimers in the Gas Phase

Åke Andersson, Mathias Poline, Kas J. Houthuijs, Rianne E. van Outersterp, Giel Berden, Jos Oomens, and Vitali Zhaunerchyk. *J. Phys. Chem. A* **125**, **34**, 7449–7456 (2021)
DOI: 10.1021/acs.jpca.1c05667

Author's contributions

PAPER I: I was in charge of the experimental beamtime at DESIREE. I developed and performed the data analysis and modeling of the DESIREE results and wrote the manuscript.

PAPER II: I was in charge of the experimental beamtime at DESIREE. I developed and performed the data analysis and modeling of the DESIREE results and wrote the manuscript.

PAPER III: I was in charge of the experimental beamtime at DESIREE. I developed and performed the data analysis and modeling of the DESIREE results and wrote the manuscript along with Nicolas Sisourat.

Summary

This thesis deals with experimental studies of electron transfer reactions between oppositely charged ions (cations and anions), in a process called mutual neutralisation. These investigations were performed at the double electrostatic ion storage ring DESIREE at Stockholm University, which was put into full operation in 2017. This unique apparatus consists of two cryogenic electrostatic rings where oppositely charged ion beams are stored and merged in a common section where the reactions of interest take place. The neutral products arising from the reactions are detected in coincidence using a sensitive 3D imaging detector. This approach allows the kinetic energy of the products to be measured, and the particular product channels to be identified, such that the branching ratio into the different competing sets of products can be determined.

In the first two published articles included in this thesis, the mutual neutralisation of atmospheric ions are treated, namely O^+/O^- (oxygen ions) and N^+/O^- (nitrogen/oxygen ions). Particular products from these reactions are expected to contribute significantly to the UV airglows observed in the F-layer of the Earth's atmosphere. The two main aims of these studies was: i) to reproduce previously reported results from a single pass (non stored) merged ion beams experimental apparatus in UCLouvain (Belgium), thus providing a measure of DESIREE's capacity and resolution, ii) to investigate the contributions of metastable ions present in the ion beams, where analysis and interpretation was undertaken with the support of theoretical calculations. The experimental spectra were found to be in good agreement, and the calculations could reproduce these results well, except for the metastable state contributions, which require more advanced and computationally expensive theoretical models.

The third published paper included in the thesis deals with collisions between I^+ and I^- (iodine ions), a process which is relevant to the use of electric thrusters as efficient engines for new spacecraft. It was found that both ground state and excited products were formed in the reaction. The experimental results were compared with theoretical calculations in order to provide an understanding of how the reaction takes place. These suggested that the charge transfer occurs at short inter-nuclear separations, through multiple avoided crossings of the ion-pair states and the covalent states. These combined data are useful for plasma modelling of these electric thrusters.

Finally, preliminary results on electron transfer reactions between the diatomic ion O_2^+ (dioxygen) cation and O^- showed that mutual neutralisation can also result in complete dissociation of the molecule, with different break-up dynamics depending on the final neutral products formed.

Sammanfattning

Denna avhandling handlar om experimentella studier av elektronöverföringsreaktioner mellan joner av motsatta laddningar (katjoner och anjoner), i en process kallad ömsesidig neutralisering. Dessa studerades vid den dubbla elektrostatiska jonlagringsringen DESIREE på Stockholm Universitet, som togs i full drift 2017. Denna unika anläggning består av två kryogena elektrostatiska ringar där motsatt laddade jonstrålar lagras och möts i en gemensam sektion där reaktionerna av intresse äger rum. De neutrala produkterna som uppstår från dessa reaktioner detekteras med hjälp av en känslig 3D-bilddetektor. Detta gör det möjligt att mäta den kinetiska energin hos produkterna, och på så sätt identifiera produktkanalerna och bestämma förgreningsförhållandet för de olika konkurrerande uppsättningar av produkter.

I de två första publicerade artiklarna inkluderade i denna avhandling, behandlas den ömsesidiga neutraliseringen av atmosfäriska joner, nämligen O^+/O^- (syrejoner) och N^+/O^- (kväve/syrejoner). Specifika produkter från dessa reaktioner förväntas bidra väsentligt till UV-glöd som observeras i F-skiktet av jordens atmosfär. De två huvudsakliga syftena med dessa studier var att: i) reproducera tidigare rapporterade resultat från en "single-pass" (icke lagrade jonstrålar) experimentell apparat i UCLouvain (Belgien), och på så sätt ge ett mått på DESIREEs kapacitet och upplösning, ii) undersöka bidragen från metastabila joner i strålarna, där analys och tolkning genomfördes med stöd av teoretiska beräkningar. De experimentella spektra visade sig stämma bra överens, och beräkningarna kunde återge dessa resultat väl, förutom för de metastabila tillståndsbidragen, som kräver mer avancerade och beräkningsmässigt dyra teoretiska modeller.

Den tredje publicerade artikeln som ingår i avhandlingen handlar om kollisioner mellan I^+ och I^- (jod-joner), en process som är relevant för användningen av elektriska jonpropeller som effektiva motorer i nya rymdfarkoster. Det visade sig att både grundtillstånd och exciterade produkter bildades i reaktionen. De experimentella resultaten jämfördes med teoretiska beräkningar för att ge en förståelse för hur reaktionen går till. Dessa antydde att laddningsöverföringen sker vid korta internukleära separationer, genom multipla undvikade korsningar mellan jonpartitillstånden och de kovalenta tillstånden. Dessa kombinerade data är användbara för plasmamodellering av elektriska jonmotorer.

Slutligen, preliminära resultat på elektronöverföringsreaktioner mellan diatomärjonen O_2^+ (syre molekyl) och O^- visade att ömsesidig neutralisering kan också resultera i dissociation av molekylerna, med olika upp-brytningsdynamik beroende på vilka produkter som bildas.

1 Introduction

1.1 Historical overview

Ionised gases, more commonly known as plasmas, are a unique state of matter in which a variety of elementary inter-particle reactions take place. These include ion-neutral electron transfer, electron attachment to neutrals, and ion recombination, all of which have been studied extensively in the past [1]. Of note, there exists over 2300 studies on ion-neutral interactions according to a literature review from 2003 [2], and decades of experimental research on collisions of electrons with atoms and molecules [3, 4]. In contrast, investigations on ion recombination reactions have largely been limited to observations and theoretical calculations, due to experimental constraints.

Prior to the development of laboratory plasmas, the only means of collecting information about these environments was through direct observation of radiation emitted from natural plasma sources, such as our own atmosphere and planetary nebulae. Initially, it was believed that the dominating ion-loss mechanism in these environments was radiative recombination (RR), a process which can be schematically written as



In this reaction, a cation is neutralised through the capture of a free electron into an excited state, and the excess energy is released through emission of a photon, providing a characteristic signature of the reaction taking place. However, it became clear early on that this simple picture was incomplete. Studies of the ionosphere suggested that other types of recombination processes were also taking place, and, in 1943, Massey and Bates [5] introduced a new type of process, namely dielectronic recombination (DiR)



In this process, the incident electron is captured into an excited state while a bound, inner-shell electron is simultaneously excited into the next open sub-shell. Stabilisation then occurs by emission of a photon when this latter electron relaxes back to its original state. As an example, figure 1.1 illustrates these two processes for a Mg^+ ion.

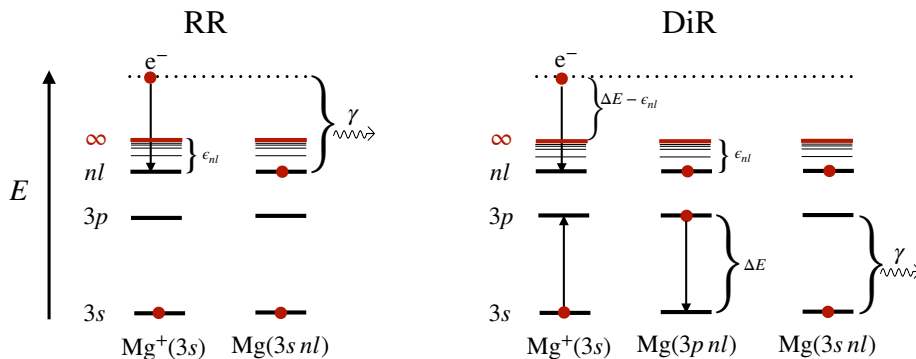


Figure 1.1: Schematic of radiative recombination (RR) and dielectronic recombination (DiR) in a Mg^+ ion.

As can be seen, while the two processes both can result in the formation of the same final neutral product and emitted photon energy, DiR can only occur if there is sufficient excess energy to produce a core-excitation, i.e., if

$$E_e + \epsilon_{nl} = \Delta E, \quad (1.3)$$

where ΔE is the excitation energy of the core electron, ϵ_{nl} is the binding energy of the Rydberg state into which the electron is captured, and E_e is the electron's kinetic energy. Therefore, DiR is a resonant process which only occurs at specific incident electron energies, and results in distinct spectral lines. In contrast, RR can result in production of photons of any wavelength, depending on the collision energy.

While RR dominates for capture into low-lying excited states, DiR is actually the main process for capture into highly excited states, due to the inherent nature of the process [6]. Eventually, it was deemed that DiR was mostly absent from our atmosphere, but was found to be particularly prevalent in hot astrophysical plasmas, such as the solar corona, where so-called ‘‘satellite lines’’ are observed in spectra taken during solar

flares [7].

On the theoretical side, several models were developed to explain the physics behind these two recombination reactions. For RR, it was relatively straight-forward, as a semi-classical formula for the inverse process, namely photo-ionization, had already been introduced in 1932 by Kramers [8]. The semi-classical cross section for capture into an electron orbital with principle quantum number n is calculated as follows:

$$\sigma_{\text{RR}} = \frac{32\pi\alpha^3}{3\sqrt{3}} \left(\frac{\eta^4 a_0^2}{n(\eta^2 + n^2)} \right). \quad (1.4)$$

Here, α is the fine-structure constant, a_0 is the bohr radius, and $\eta = \sqrt{I_Z/E_e}$ [9], where I_Z is the ionization threshold energy of the atom. Subsequent quantum mechanical calculations lead to the addition of a ‘‘Gaunt factor’’ to take into account the orbital angular momentum degeneracy, and more generalized formulas were derived to calculate total RR rates taking into account all electronic states and relativistic effects [10].

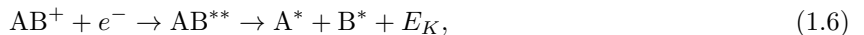
For DiR, the process is more complicated, as the first step is reversible. This means that the excited species formed in the initial capture step is unstable, and might autoionize. Furthermore, as mentioned earlier, it is a resonant process. The cross section is then given by [11]

$$\sigma_{\text{DiR}} = \frac{S}{\pi} \frac{\Gamma/2}{(E_e - (\Delta E - \epsilon_{nl}))^2 + \Gamma^2/4}. \quad (1.5)$$

where S (eV/cm²) is the survival factor, which comprises the rate of autoionization as well as the multiplicity of the initial and intermediary states, and Γ is the resonance natural width of the doubly excited state.

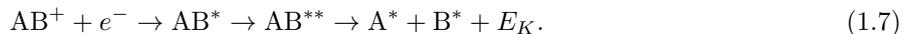
With these tools in hands, theoreticians could then derive complete sets of RR and DiR rate coefficients over wide range of temperatures for use in plasma modeling [12, 13].

In parallel to this ongoing research on atomic ions, growing interest was developing in the study of the recombination of molecular ions. It was discovered quite early on [14] that such processes often resulted in breaking of molecular bonds. This dissociation was not caused by the collision itself but by the capture of the electron into a doubly excited state with a repulsive potential energy curve, i.e



where E_K is the kinetic energy released in the reaction, and A and B are the resulting neutrals, which can be either formed in their ground state or any energetically allowed excited state. This reaction, known as dissociative recombination (DR), generally occurs at crossings between the ionic state and an excited neutral state. As the electron is typically captured into a highly vibronically excited state of the neutral molecule, the molecular bond starts to stretch, and the molecule ends up dissociating into the two neutral products.

As in the atomic case, it was found that a two-step process via a Rydberg-state could also occur, i.e:



The latter was therefore named indirect dissociative recombination (IDR), as opposed to the former, direct process (DDR).

To explain these two distinct reaction pathways, let us illustrate with an example: Figure 1.2(a) shows a few selected potential energy curves relevant to the DR of O_2^+ . The ground state ionic curve $\text{O}_2^+(X^2\Pi_g)$ (here shown in black) crosses the two dissociative states, $\text{O}_2^{**}(^1\Sigma_u^+)$ (blue curve) and $\text{O}_2^{**}(^1\Delta_u)$ (red curve), at an internuclear distance of about ~ 2.4 Bohr radii. The two states have different dissociation limits, and so the final products electronic states and kinetic energy will depend on which pathway the reaction follows.

Now, let us look at the process in more detail. Figure 1.2(b) shows a zoomed in view of the potential surfaces around the crossing region, with some relevant vibrational states highlighted. The ionic curve $\text{O}_2^+(X^2\Pi_g)$ is found to cross the doubly excited dissociative state $\text{O}_2^{**}(^1\Delta_u)$ (red curve) even in its lowest vibrational state, and thus a direct transition (DDR) is possible, as illustrated by the red arrow (note that the arrow then corresponds to a specific electron energy E_e). Conversely, the $(^1\Sigma_u^+)$ dissociative state (blue curve) is not directly accessible, at least not in the electron energy range considered here. However the transition may occur indirectly (IDR) through a vibrationally excited Rydberg state $\text{O}_2^*(^1\Sigma_u^+ \text{ Ryd})$ (dashed line), as

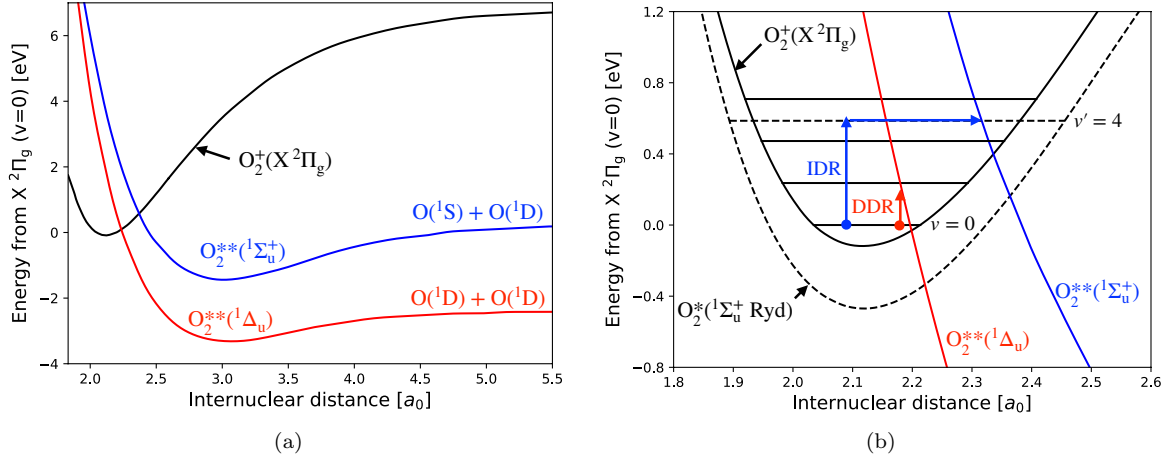


Figure 1.2: (a) Several relevant potential energy curves in the DR of O_2^+ . (b) Schematic of the indirect (IDR) and direct (DDR) dissociative recombination reactions in O_2^+ . Adapted from Guberman [15, 16]

indicated by the blue arrows. Since this state does cross the potential energy curve, a transition to the dissociative state $^1\Sigma_u^+$ is now possible. This is particularly relevant in the DR of O_2^+ with low-energy electrons, as this is the only accessible state which can yield $O(^1S)$ excited neutrals. This indirect process is therefore believed to be the dominant production route of $O(^1S)$ in our atmosphere [16, 17].

Similarly to dielectronic recombination, IDR is a resonant process since it can only occur at electron energies where capture into a Rydberg state is possible. Competition with the direct process can also happen, which then results in resonances in the cross section, as it has been observed, for example, in the DR of H_2^+ [18]. An expression for the DR cross section is given by [19]:

$$\sigma = \frac{\Gamma[FC]S}{E_e}, \quad (1.8)$$

where E_e is the incident electron's energy, Γ the natural resonance width, and FC is the Franck-Condon factor, which describes the overlap between the vibrational wavefunctions of the two states involved. As mentioned previously, the survival factor, S , is a measure of the probability that the initial excited state formed in the capture event remains on this potential energy curve, and doesn't autoionize.

However, ions do not only recombine with free electrons. Negative ions are also highly prevalent in many plasmas as electrons react with any particle they encounter. The recombination of oppositely charged ions, the subject of this thesis, is what is known as mutual neutralisation (MN).



where the excess energy is, similarly to DR, distributed into excitation energy (*) and kinetic energy E_K .

Each reaction considered so far has been associated with an additional level of complexity, both in the theoretical treatment, and the experimental techniques required to study it. It is therefore not surprising that MN is the least well known of the main plasma reactions. Indeed, for an experimental probing of the MN reaction, one must be able to produce both positive and negative ions, confine them in an interaction region, and be able to distinguish the reaction from other recombination processes.

From a theoretical perspective, MN shares some similarities to DR as it also occurs at curve crossings between ionic and covalent states. However, since the MN system starts from two ions at infinite distance, the transition can already occur at large internuclear separations, and the theoretical treatment differs in many aspects. The dynamics are generally simplified and described by the Landau-Zener model [20, 21], dating from 1932, which gives the diabatic transition probability in a two-state quantum system:

$$P_D = e^{-2\pi H_{12}^2/\hbar a}, \quad (1.10)$$

where a is a constant, and H_{12} is the non-diagonal element in the system's Hamiltonian. The latter is often non trivial to calculate, as it requires evaluating the relevant wavefunctions, which may be done using ab

initio methods or semi-empirical formulas. In the case where MN involves a molecular ion, i.e:



then the theoretical treatment becomes even more complicated, as one must take into account the angle between the two reactants and compute the contributions from each molecular state. To the best of our knowledge, no such calculations have been reported so far on MN system involving molecular ions, and knowledge on the reaction rely largely on experimental data.

Historically, two types of apparatus have been mainly used for the study of recombination reactions: Flowing Afterglow (FA) and Interacting Beams (IB).

In FA, a carrier plasma of an inert gas is created in a glow discharge and moved through a flow tube by an electric field [22]. Further down the tube, the ions of interests are formed through reactions with the carrier gas and possibly other molecules introduced. The recombination reactions then take place in an interaction region further downstream and a mass spectrometer at the end of the flow tube detect the ions in order to determine the reaction rates. The setup can be improved by the introduction of a movable electrostatic probe (Langmuir Probe) [23], which allows to measure the ion and electron density along the tube. From the rate-of-loss, one can then, based on the plasma flow speed, calculate recombination rate coefficients with great accuracy. However, the FA method has significant drawbacks: It is often difficult to determine the constituents of the gas, i.e., what partners are reacting to give the observed loss of charged particles. The detection of the neutral products in such recombination reactions also involve complex schemes such as re-ionization by electron impact prior to the mass spectrometer and laser-induced fluorescence measurements targeting specific products [24]. In addition, the resulting fragments can be difficult to distinguish from background reactions involving ions which are naturally present in afterglow plasmas.

In IB apparatus, there is no carrier gas, and, instead, the charged species are produced independently, mass-selected, and then confined into mono-energetic beams. As such, this technique is generally more reliable since the interacting species are well known. The two beams are then made to interact, typically in a high vacuum region, and a neutral-particle detector is used to monitor the reaction products in order to evaluate the reaction rates. The first IB investigations were reported in the late 1960s, with the study of the fundamental reaction H^+/H^- , i.e



At the time, it was not clear which type of beam interaction method was the most suitable and various techniques were used to measure the reaction. The crossed-beam configuration [25] (i.e., with the ion beams perpendicular to each other) offered the advantages of providing a well defined collision region, but was limited in terms of collision energies achievable. In contrast, in the merged-beam configuration (i.e., with the ion beams superimposed) [26, 27], the two beams could be set to the same velocity such that a very low collision energy could be achieved, and a longer interaction region and greater resolution could be obtained. However, there were major difficulties in distinguishing MN from other type of ion-loss processes, for examples:



A compromise of the two configurations, the “inclined beam technique”, in which the two beams are crossed at a small angle, was subsequently used [28, 29], and provided satisfying results. Subsequent technical developments in the 1980s, e.g. implementation of single particle detectors and coincidence techniques, made it eventually possible to discriminate other reactions, and the merged beam configuration became soon the technique of choice [30–32].

In the four recombination reactions mentioned so far (RR, DiR, DR, and MN), there is one very important aspect which has not yet been considered: the reaction rates inevitably depend on the electronic, vibrational, and rotational distributions of the reacting ions. As such, in order for the experiments to be relevant for atmospheric and astrophysical applications, one must ensure that the ions studied in laboratory are at low temperature. In FA apparatus, the ions and electrons thermalise through interactions with the carrier gas and collisional quenching, such that the studied species are typically at room temperature as they reach the interaction region. In IB machines, this is more complicated to achieve as one must either

use special ion sources, or employ trapping methods. One particular method to address the latter is ion storage rings.

The utilisation of ion storage rings for the purpose of studying recombination reactions began in the late 1980s. Of note, the Test Storage Ring (TSR) in Heidelberg started its operation in 1988 [33], later followed by the Aarhus Storage Ring in Denmark (ASTRID) [34], and the Crysis Synchrotron Ring (CRYRING) [35] in Stockholm, both in 1991. In essence, the three facilities are based on the same principle: Ions are produced externally, guided to the storage ring where they are accelerated to high energies (typically MeV), whilst being confined in the ring, i.e. they operate as synchrotrons. Whilst stored in the ring, infra-red active ions cool down radiatively from their ro-vibronically excited states.

For collisions with free electrons, an electron cooler is present in one of the sections of the storage ring. This device produces a mono-energetic dense electron beam, which is then guided into the storage ring, where it is merged with the beam of stored ions to serve as an electron target, before the electrons are guided back out of the ring. In this interaction region, reactions between the ions and free electrons take place. Neutral products produced in these reactions continue on a straight path out of the ring where they are monitored by different types of particle detectors. Different data analysis techniques are then used to identify the nature and energy of these products. One of the significant advantages of ion-storage devices over single-pass interacting beams machines is that ions which do not react in the interaction region remain stored, and, as such, will re-enter the interaction region after travelling around the ring, and so more efficient use is made of the ions.

However, and of relevance here, these apparatus could only study recombination reaction with free electrons, as the study of MN reactions would then require an additional storage ring for the anions. It therefore took close to 30 years before the first double storage ion ring was eventually developed. Denoted DESIREE [36, 37] (Double ElectroStatic Ion-Ring ExpERiment), the apparatus is the only merged beams setup where both ions are stored prior to interaction. Its cryogenic and ultra high vacuum properties allows to study MN reactions involving ions in their lowest quantum states. Located at Stockholm University, it became an international facility in 2015, with the first merged beams results published in 2020[38].

1.2 MN in planetary atmospheres

Typically, plasmas are thought of as highly energetic gases only present in extreme conditions. However, large parts of our own atmosphere can actually be described as cold plasmas, as many ionized species are prevalent there. The presence of these ions is mainly due to the constant influx of radiation from cosmic rays and from our Sun, in the form of UV photons. The latter are often categorized according to their wavelengths, denoted by the letters A to C, in increasing energy. The UV-C photons are typically in the 100-280 nm range, corresponding to 4-12 eV energy, which is sufficient to dissociate the molecular bonds of the most prevalent gases, namely nitrogen and oxygen.

As such, in the upper atmosphere (≥ 300 -800 km), these mainly exist as atomic species, and reactions involving the atomic ions determine the charge-state balance and neutral densities. Furthermore, the excited neutrals formed in these reactions de-excite through spontaneous emissions of photons, resulting in airglows. For example, in oxygen, the 135.6 nm emission line is one of the primary means of quantification of ionospheric plasmas[39]. The primary mechanism for the productions of these photons occurs through radiative recombination (RR)[40]



However, the free electrons present there may also attach to neutrals, resulting in oxygen anions:



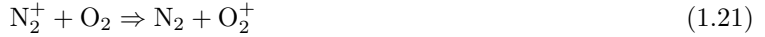
Consequently, reactions between the two oppositely charged oxygen ions may occur, i.e, mutual neutralisation.



While this process is less probable due to the intermediary steps required, it is a much more efficient process. Rate constants for radiative recombination reactions are typically small, in the order of 10^{-12} cm³/s or less [13], while those of MN can be as high as 10^{-7} cm³/s. As such, it is estimated that MN could contribute

up to 40% of the observed 135.6 nm emission in the nightsky [39].

At lower altitudes (100-300 km), the remaining radiation is less energetic, due to the absorption from the F layer and the higher pressure, and molecular species dominate. While N_2 is the most prevalent molecule, the ion readily reacts with oxygen to form NO^+ and O_2^+ [2].



Here, dissociative recombination of these two ions starts to become important (equation 1.6,1.7), though mutual neutralisation also has some relevance (equation 1.11). Since some of the available reaction energy goes into the breaking of the bond, the neutral products are generally formed in lower excited states than in the neutralisation of atomic ions. Two emission lines then dominate at these altitudes, namely $O(^1S \rightarrow ^1D)$ at 557.7 nm (as mentioned earlier in connection to Figure 1.2), and $O(^1D \rightarrow ^3P)$ at ~ 633 nm. Those are both in the visible spectrum, and are known as the airglow green line and red lines, which are observable in the night sky.

Below 100 km altitude, the density of particles gradually increases and negative charges are mostly carried by ions. Mutual neutralisation becomes a competitive process again, though it generally involves more complex ions, such as hydrated molecules and small clusters [41]. The rates and products are then mostly unknown due to the lack of experimental and theoretical data.

These charge reducing reactions are not only relevant to Earth. All planetary atmospheres contain ions, and study of these charge-reducing mechanisms can help not only determine the history and evolution of these atmospheres, they can also provide clues as to processes occurring on the planet. Several planets and planetary bodies in our solar system are believed to have lost large parts of their atmosphere over the past million years. These losses have a number of causes, which include photoionization as well as dissociative recombination and mutual neutralisation, as the neutral products formed in these reactions acquire significant kinetic energy in the process which can be sufficient to reach escape velocity and escape the atmosphere. For example, on Mars, dissociative recombination of molecular oxygen and nitrogen results in fast fragments, sometimes exceeding the escape velocity, and as a consequence, the heavier isotopes of these atoms are found in higher concentrations in the martian atmosphere compared to that of our own [42]. Similarly, on Venus, recombination reactions of O_2^+ result in energetic oxygen atoms which reacts with hydrogen, resulting in high rates of atmospheric hydrogen escape [43]. Even Saturn's moon Titan, has been revealed to contain a dense atmosphere with complex positive/negative ion chemistry, which is favourable to MN [44].

1.3 MN in industrial and applied plasmas

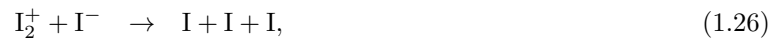
Historically, study of recombination reactions have been mainly focusing on naturally occurring plasma, such as the ones mentioned before. In recent years, there has been growing interest in plasma technology for industrial use, e.g. in combustion engines and energy storage[45]. However, research is highly needed in the recombination reactions taking place and their effects on these plasmas. For example, in air-plasma assisted combustion engines, the nature and the concentration of ionic species are believed to play an important role in the diagnostics and properties of these devices. Optimising and modelling the ignition process is crucial and proves a considerable challenge to understanding the increased efficiency due to the unknown effects from electrons/anions and their interactions with positively charged plasma constituents [46].

In supersonic vehicles, the introduction of a plasma torch is found to result in reduction of the ignition delay time and an increase of the efficiency of the engine [47]. A possible explanation for this, is the recombination of hydrocarbon ions which is known to result in production of radical species, e.g. [48, 49] :



These formed radicals could then help initiate and propagate the combustion reaction, resulting in the observed increase in performance.

In electric thrusters, the acceleration is entirely driven by the ions, which are formed by electron bombardment to produce a plasma. In recent years, iodine has been considered to be an attractive choice for a propellant [50], due to its low density and high availability. However, in contrast to xenon, iodine is reactive, and thus charge transfer reactions are expected to affect the efficiency of the engine. Recent modeling suggests that the MN reactions



may be important to the performance of these thrusters [51]. These are expected to be a source of power loss, due to the loss of ions available for propulsion. Furthermore, the neutrals produced in these reaction may undergo further reactions which could also affect the efficiency of the engines.

2 Experimental apparatus

All the experiments were carried out at the double storage ring facility DESIREE (Double ElectroStatic Ion-Ring ExpERiment) located at Stockholm University. DESIREE is a unique ion beam storage apparatus in which two oppositely charged ions can be stored simultaneously in two separate rings with a common merged section[36, 37]. There are two main advantages of this machine: i) It is electrostatic, which means the storage is mass-independent and there are no perturbation from magnetic fields; ii) It is cryogenic, which implies an ultra high vacuum and a low amount of blackbody radiation, such that there is very little perturbation from residual particles or blackbody photons.

In single ring operation, DESIREE can be used to study atomic and molecular relaxation processes down to their lowest quantum states. For example, rotational cooling of the OH anion could be achieved down to a 95% ground state population, corresponding to a temperature of 20K, allowing to determine the intrinsic rotational cooling lifetimes[52]. In double ring operation, DESIREE functions as a merged-beams setup, as described in the previous section, with the unique difference that the ions are stored, allowing to study MN reactions as a function of the temperature of the ions.

Operation of DESIREE as a merged-beam setup can be divided into three parts: (i) ion production and injection, which is crucial in order to obtain ion beams with well defined energies and masses; (ii) ion storage, which comprises beam monitoring and all the necessary steps in order to obtain parallel overlapping beams at well-defined collision energies; (iii) the detection system, which allows to detect the resulting products from the reactions under investigation.

2.1 Ion production

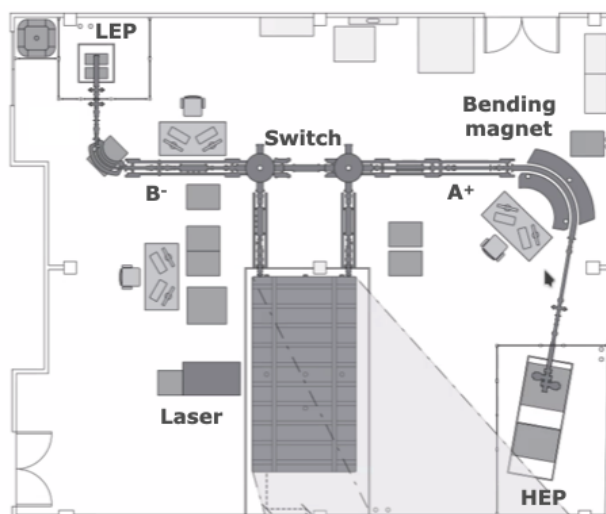


Figure 2.1: Overview of the ion production and injection at DESIREE. The positive/negative ions are generally produced at the high-energy platform (HEP) and low energy platform (LEP) respectively, mass-selected at the bending magnets, and injected into DESIREE

The production of all of the positive ions discussed in this thesis takes place on the high-energy platform (HEP) (see Figure 2.1), where ions can be accelerated up to 100 keV. Production of the negative ions takes place on the low-energy platform (LEP) which is limited to a maximum beam energy of 30 keV. On the HEP, multiple ion sources are available, and these mostly use electron impact to ionize the sample gas of interest. In the experiments described in this thesis, an ECR (Electron-cyclotron-resonance) ion source was often the choice of preference, since it can produce stable ion beams of practically any element that can be brought into the gas-phase. An ECR makes use of magnetic fields and microwave radiation to confine energetic electrons, which are then used to ionize the sample gases introduced into the source[53]. Another commonly used source is a Nielsen ion source [54], which makes use of a filament to produce electrons via thermionic emission. These are accelerated by an anode voltage, and confined by a solenoid magnetic field, where they ionize the injected sample gas.

The negative ions are generally produced in a cesium-sputtering SNICS source [55]. Cesium metal is heated in an oven, and the vapour is introduced into the ion source. The cesium vapour hits the surface of the ionizer where it is ionised through surface ionisation. The cesium ions are then accelerated towards a negatively biased cathode made of an appropriate target. The cesium ions impact the material, and material in the cathode is sputtered out. On passing through and interacting the deposited cesium, the sputtered material can pick up an electron to form an anion. These negative ions are then accelerated away from the cathode.

The positive or negative ions created in the ion sources are extracted out of the source, and then accelerated into the beam lines. After extraction off the platform, the ions reach a bending magnet (as shown in Figure 2.1), which is used to select ions according to their mass-to-charge ratio with a high precision. In standard operation, and after this selection, the positive ions are injected into the high-energy ring, and the negative ions into the low-energy ring. However, in some circumstances, the mass and energies of the ions are such that the negative ions are more energetic. In such cases, the more energetic ions are injected into the high-energy ring.

2.2 The ion storage rings

The two storage rings and the associated ion optics are all enclosed in a double-walled vacuum chamber. The outer chamber is composed of steel plates welded together, amounting to a total of 5 tons. This structure is not only necessary to preserve the vacuum inside the chamber but also to withstand the pressure differential created across the walls when everything is pumped down and cold. The inner chamber, which contains all the ion optics, the detectors, and where the ions are stored, is made of a special aluminium alloy. To provide thermal insulation between the inner and outer chambers, the inner chamber is covered with a thin shield made of copper and then covered with 30 layers of super insulation. These choice of materials used is due to their high thermal conductivity, which is crucial in order to allow heat to be effectively pumped out from the inner chamber and to reduce the effect of the room-temperature black-body radiation from the outer vessel which is continuously heating the inner chamber. On the bottom of the vessel, four closed-circuit cryocoolers are used to effectively cool the copper shield to 60 K and the inner chamber to ~ 14 K. The combination of cryo-cooling, with turbo-pumps, getter-pumps, and ion-pumps, means that the residual gas number density in the inner chamber is kept between 10^3 - 10^4 cm^{-3} , which corresponds to a room-temperature-equivalent pressure of 10^{-14} mbar [36, 37].

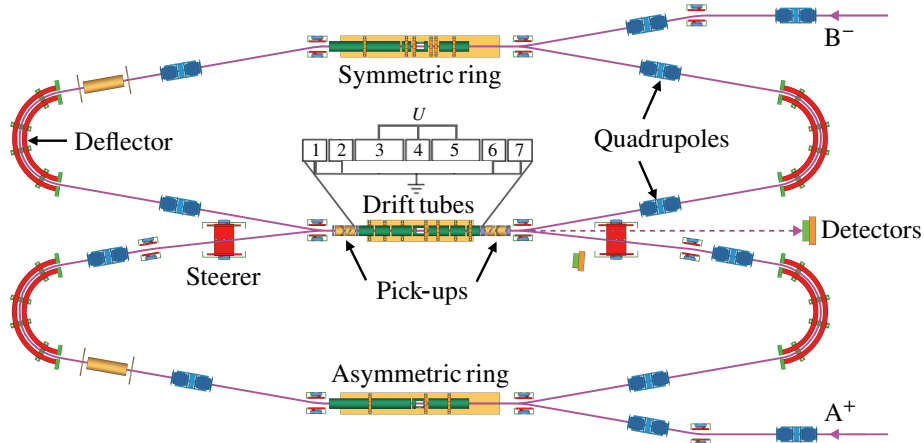


Figure 2.2: Overview of the double storage ring setup at DESIREE. The two oppositely charged ion beams A^+ and B^- enter the storage rings and are merged into a common section (Drift tubes), where a voltage U is applied to control the collision energy.

A schematic of the double ion storage rings and their common merging section is shown in Figure 2.2. The positive (A^+) and negative (B^-) ions are guided to the entrance of their respective rings by electrostatic ion optics. Quadrupoles are used to focus the beams, and deflectors are used to keep the ions on a stable orbit around the rings. The ion-optical elements are distributed differently among the two rings, in a "symmetric" or "asymmetric" arrangement, and this is used to denote the two rings. This particular

arrangement allows merging ion beams of different energies into the common straight section. Pick-up electrodes, located at the entrance and exit of the drift tube region, measure the currents of the ion beams. Given the beam velocity and the pick-up currents, the position of the ions as they pass through the merging region can be determined, and this allows us to control the overlap of the two beams to high precision.

The merging region consists of seven drift tubes, numbered according to the inset schematic shown in Figure 2.2. Each drift tube can be controlled independently or they can be coupled together to the same power supply. A voltage, U , applied to a selection of drift tubes (here 3,4,5 as an example) accelerates/decelerates the ions depending on their charge, which allows to fine tune the collision energy $E_{c,m}$, according to:

$$E_{c,m} = \mu \left[\frac{E_1 - q_1 U}{m_1} + \frac{E_2 + q_2 U}{m_2} - 2 \sqrt{\frac{(E_1 - q_1 U)(E_2 + q_2 U)}{m_1 m_2}} \cos \alpha \right], \quad (2.1)$$

where E_n, q_n, m_n are the beam energies, charge-state, and masses of the cation ($n=1$) and anion ($n=2$), respectively, and α is the angle between the two beams. In the grounded region (in the example shown in Figure 2.2, this is drift tubes 1,2,6, and 7) the voltage U is set to zero, and the collision energy is therefore much higher since the beam velocities are not matched. Neutrals produced in the MN reactions continue on a straight path to the detection system located at about 1.7 meters from the center of the merging section (drift tube 4).

The advantage of an ion storage ring such as DESIREE is that un-reacted ions continue circulating in their respective rings, and are repeatedly merged in the common section. Since these are stored in an ultra high vacuum, collisional destruction with the remaining residual gas particles is greatly reduced, and the ions may have sufficient time to relax from their initial electronic, rotational and vibrational excited state population, where, via coupling with the environment, they can undergo radiative cooling.

Typical storage lifetimes for merged-beams are of the order of 10-60 seconds. The lifetime is due to ion-loss mechanisms such as collisions with residual gas particles and ions which end up on unstable orbits. Storage times commensurate to this lifetime are therefore typically chosen in order to maintain a useful count rate. At the end of the storage period, the deflectors are switched to injection mode, resulting in dumping of the ions. The rings are then reset, and new ion bunches are injected into the storage rings to start a new measurement cycle. This procedure is repeated for many such measurement cycles, in order to investigate storage-time-dependent behaviour, and to obtain enough statistics to allow analysis.

2.3 Detection system

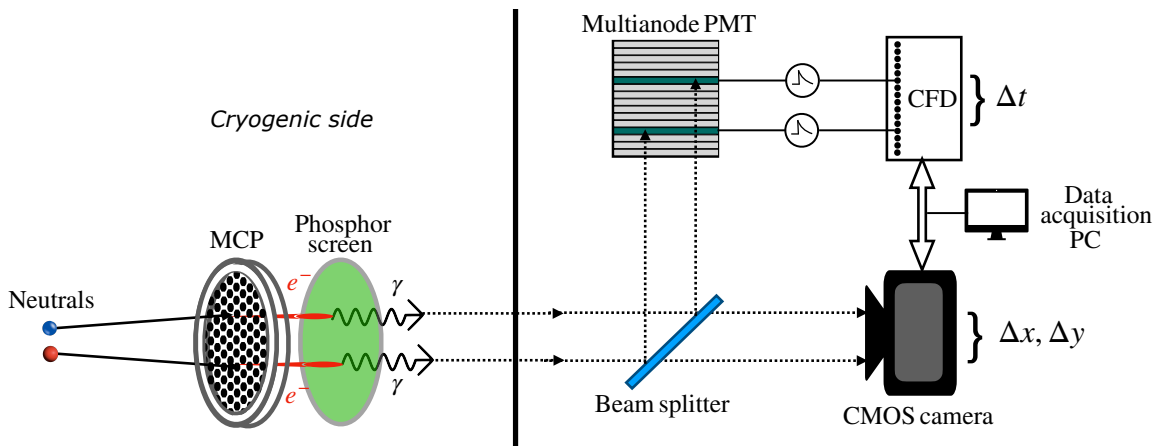


Figure 2.3: Schematic of the detectors and data acquisition system at DESIREE.

In order to detect neutrals resulting from MN reactions, a triple-stack microchannel plate-based detector (MCP) coupled to a phosphor screen anode is used [56]. The MCP functions as a particle multiplier, creating a localized cloud of electrons at the position where the detected particle hit the surface of the plate. The use of three-plates in a Z-stack configuration provides further amplification, allowing for high sensitivity, while preventing propagation of ions generated by the incident particles. At the backside of the last plate,

the cloud of electrons exiting the channels are accelerated towards the phosphor screen. The electrons excite the phosphor, resulting in emission of photons which are then focused using lenses and guided out of the cryogenic inner chamber, through the screens and the outer box, to a beam-splitter where they are then sent to the detection system. Figure 2.3 shows a rough schematic of the process. The CMOS camera (complementary metal oxide semiconductor) captures the transmitted light, and the software records the positions, intensities and sizes of the spots, obtained during each 1 ms exposure.

For many years, technical limitations restricted imaging measurements to two dimensions, since arrival time differences between products from merged-beam apparatus are typically in the nanosecond range. In contrast, the two-dimensional impact separation of the products on the detector surface are of the order of millimeters, which most position sensitive detectors can determine with high precision. This is important, as the observed distribution of the neutrals on the detector surface is often used to evaluate the kinetic energy release distribution. However, since this projected separation depends on the angular distribution of the products, which is generally unknown, several parameters must be fitted simultaneously to the data, which can introduce some uncertainties into the analysis.

The implementation of the third dimensional component, namely time, in this type of imaging technique was first introduced by Amitay and Zajfman [57] for the study of dissociative recombination reactions, by implementation of an advanced multi-anode photo-multiplier (PMT) to the detection system. At DESIREE, the same principle is used, and the phosphor screen is imaged onto both the camera and the PMT. Light flashes from the phosphor are then registered in both the camera and trigger anodes in the PMT, the latter producing a timing signal from each light-spot.

Each time a PMT channel is triggered, a signal is sent to the constant fraction discriminator (CFD). The first detected signal also triggers a common stop signal, typically corresponding to a 200 ns time window. All signals recorded within that time window are therefore recorded and transcribed to digital values by an analog-to-digital converter. The two detectors are controlled simultaneously by the data acquisition computer, which records the measured values on an event-by-event basis. The obtained values are then converted based on a calibration measurement where the ADC is fed pulses of specific values which duration are measured using an oscilloscope. The relation between the two is linear, and in principle the arrival time differences can be determined to a precision of 0.1 ns. However, the experienced delays of each channel are observed to vary, requiring an additional correction, and the actual resolution is likely of the order of 1 ns.

3 Data Analysis

The displacement of the products in the center of mass frame is directly related to the kinetic energy release, E_K , through the relation:

$$E_K = \frac{1}{2} \sum_i m_i v_i^2 = \frac{1}{2T^2} \sum_i m_i (\Delta x_i^2 + \Delta y_i^2 + \Delta z_i^2) \quad (3.1)$$

where T is the time of flight of the particles to the detector, and $\Delta x_i, \Delta y_i, \Delta z_i$ are the displacement in Cartesian coordinates of each particle from the center-of-mass. This kinetic energy release results from the excess energy of the reaction. For MN to take place, the gain of energy from neutralisation of the cation, i.e. the ionisation energy of the neutral parent (IE), must be larger than the energy required to remove the electron from the anion, determined by the electron affinity (EA) of the parent atom:

$$E_K = \text{IE} - \text{EA} - \Delta E_{\text{int}} \quad (3.2)$$

Here, ΔE_{int} is the difference in internal energy between the reactants and the products, which includes electronic excitation in atoms, as well as rovibronic excitation in molecules. Therefore, this measured energy E_K can be used to determine the initial and final quantum states of the species involved.

3.1 Preliminary data evaluation

The image-data evaluated by the camera-control software consists of the center x- and y-positions of the spots, as well as their integrated intensities and sizes. The cycle number, the identification number (ID) for the frame, and a time stamp corresponding to the time within the measurement cycle when the image was taken, are also recorded. The data from the PMT consists of time values from each of the 16 anodes, the corresponding cycle number, and the frame ID.

In the preliminary data evaluation, a matching algorithm is used to combine the data files according to their frame ID and cycle number. This process can sometimes be quite tedious as offsets in the cycle number and/or the frame ID can occur due to detector and communication issues. Details of the assignment method is explained elsewhere [58]. After this initial processing, a single file containing the imaging and timing information for each event is obtained. However, each event also consists of one or more particles detected in each detection system, and these must be also correlated.

The first task is to determine the number of particles which were actually observed by the multi-anode PMT. The photons emitted from the spots on the phosphor screen may trigger several adjacent anodes in the PMT, resulting in an apparent excess of detected particles. To correct for this, the differences in time between each of the 16 channels is taken, and values smaller than 5 ns for adjacent channels are categorized as arising from the same particle. The average value of the times determined for the adjacent channels is taken as the correct time.

The second task is to match these timing events to the positions recorded by the camera. MN events typically occur within a time window of a few hundred ns, which the PMTs can be programmed to measure. However, the camera cannot, as each frame is integrated for 1 ms. As such, additional events which are not related to a specific MN interaction may be recorded, for examples, products from collisions of the ions with the residual gas particles or, in rare cases where there are high ion-beam currents, products from multiple unrelated MN events. In order to match the events correctly, the recorded vertical positions of the measured spots are matched with the calibrated positions of the anodes in the PMT with respect to where on the phosphor screen they are observed.

After this selection, a complete data set with an equal number of events with position and time information is obtained, and a three dimensional reconstruction of that particular event can be made. These procedures differ depending on the number of particles produced in the MN reaction, and are therefore treated separately here.

3.2 Two particle imaging

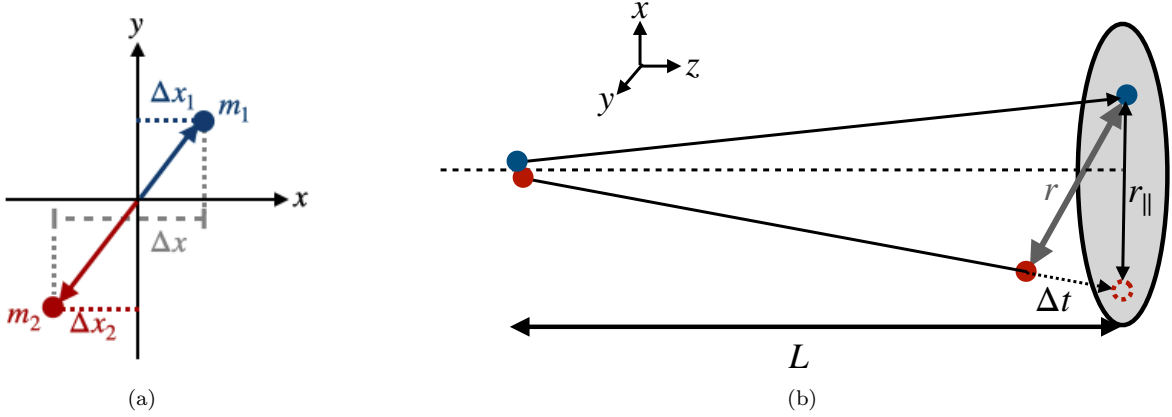


Figure 3.1: (a) Schematic of the two-dimensional displacements of two particles, and the quantities described in the text. (b) Schematic of the measured quantities.

In the case where the MN reaction results in two products, the kinetic energy released E_K in the reaction can directly be expressed in terms of the separation in position and in time of the products. From momentum conservation it follows that the displacement in the x-axis is given by $\Delta x_1 = \frac{m_2}{m_1+m_2} \Delta x$, where Δx is the separation along the x-axis of the two particles, as illustrated in Figure 3.1(a). The same holds true for Δy and Δz , and, therefore:

$$E_K = \frac{1}{2T^2} \frac{m_1 m_2}{m_1 + m_2} (\Delta x^2 + \Delta y^2 + \Delta z^2), \quad (3.3)$$

where T is the time of flight to the detector. If one selects z as the beam axis, as illustrated in Figure 3.1(b), then $\Delta x^2 + \Delta y^2$ can be approximated as r_{\parallel}^2 , the measured projected distance (squared) between the two particles on the imaging detector. Δz can be directly related to the difference in arrival time between the two particles, and be approximated as $v\Delta t$, where v is the average velocity of the two beams. The following expression is obtained:

$$E \approx \frac{\mu v^2}{2L^2} (r_{\parallel}^2 + v^2 \Delta t^2). \quad (3.4)$$

Here, we use that $\mu = \frac{m_1 m_2}{m_1 + m_2}$ is the reduced mass of the two particles, and that the time of flight can be expressed as L/v , where L is the distance from the MN event to the detector. It is now useful to define the quantity r as:

$$r \equiv \sqrt{r_{\parallel}^2 + (v\Delta t)^2} \approx \sqrt{\frac{2E}{\mu} \frac{L}{v}} \quad (3.5)$$

As can be seen in Figure 3.1(b), r corresponds to the 3D separation of the two products at the time where the first particle hits the detector. It doesn't require any identification of the products, it can be computed directly from the experimental data, and it is proportional to the square root of the energy. Since this is what is measured in laboratory, it is more convenient to use and evaluate its distribution. However, a number of experimental aspects give rise to limitations which affects the resolution of the data, and these must be taken into consideration.

Since the particles aren't measured simultaneously, the measured projected distance is not a true measure of their displacement in the x-y plane. Furthermore, the distance to the point of interaction, L , is not known exactly: It is taken to be the distance from the detector to the central point in the interaction region (i.e. the biased region). Finally, the two ions are assumed to have the same velocity prior to the reaction, which is not always true. It is therefore crucial to make proper simulations of these quantities in order to be able to interpret the experimental data correctly.

3.3 Two particle simulations

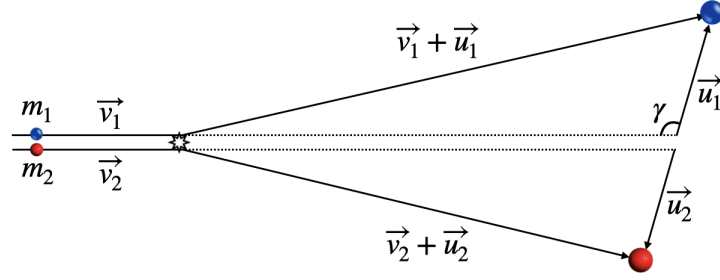


Figure 3.2: Sketch of the dynamics of the reactions and the relevant vectors for the simulation of two products from a MN reaction.

In order to model the dynamics of the MN reaction, one must determine the final velocity vectors of the two products, as illustrated in Figure 3.2. At 0 eV center-of-mass collision energy, the two ions have the same velocity prior to the reaction, i.e $\vec{v}_1 = \vec{v}_2$. The derivation is then straightforward: If one defines \vec{u}_1 and \vec{u}_2 as the additional velocity components acquired upon the reaction due to the kinetic energy released, then, from conservation of energy and momentum, the following expressions are obtained

$$m_1 \vec{u}_1 = -m_2 \vec{u}_2 \quad E_K = \frac{1}{2} m_1 \vec{u}_2^2 + \frac{1}{2} m_2 \vec{u}_2^2. \quad (3.6)$$

This allows us to solve for the vectors \vec{u}_1 and \vec{u}_2 :

$$|\vec{u}_1| = \frac{1}{m_1} \sqrt{2\mu E_K}, \quad |\vec{u}_2| = \frac{1}{m_2} \sqrt{2\mu E_K}. \quad (3.7)$$

where μ is the reduced mass.

These vectors can be decomposed into an axial component, i.e along the beam axis, and a radial component parallel to the detector plane.

$$\vec{u}_{\text{axial } 1} = \frac{\cos \gamma}{m_1} \sqrt{2\mu E_K}, \quad \vec{u}_{\text{radial } 1} = \frac{\sin \gamma}{m_1} \sqrt{2\mu E_K} \quad (3.8)$$

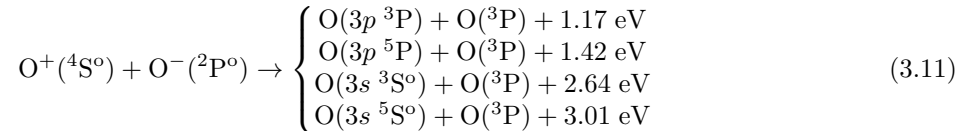
$$\vec{u}_{\text{axial } 2} = \frac{-\cos \gamma}{m_2} \sqrt{2\mu E_K}, \quad \vec{u}_{\text{radial } 2} = \frac{-\sin \gamma}{m_2} \sqrt{2\mu E_K}, \quad (3.9)$$

where γ is the angle between the beam axis and \vec{u}_1 , as illustrated in Figure 3.2. Due to the cylindrical symmetry of the reaction, $\cos \gamma$ is uniformly distributed between -1 and 1. From these two vectors, one can then calculate the measured experimental quantities:

$$\Delta t = \frac{L}{\vec{u}_{\text{axial } 1}} - \frac{L}{\vec{u}_{\text{axial } 2}} \quad r_{\parallel} = \left| L \frac{\vec{u}_{\text{radial } 1}}{\vec{u}_{\text{axial } 1}} \right| + \left| L \frac{\vec{u}_{\text{radial } 2}}{\vec{u}_{\text{axial } 2}} \right|. \quad (3.10)$$

The resulting r values may then be computed using equation 3.5.

Let us illustrate with an example. In the MN of O^+ with O^- , there are four product channels which are known to be populated in low-energy collisions [59, 60]:



In the experiment at DESIREE (Paper I), the ions were accelerated to kinetic energies of $E_1 = 8.28$ keV and $E_2 = 7.16$ keV for the cation and anion beams respectively. The ion beam velocities as a function of the applied voltage, U , are then given by:

$$v_1 = \sqrt{\frac{2E_1 - eU}{m_1}}, \quad v_2 = \sqrt{\frac{2E_1 + eU}{m_2}} \quad (3.12)$$

The voltage necessary to apply to the drift tubes in order to have matching velocities is simply obtained as:

$$U_0 = \frac{E_1 m_2 - E_2 m_1}{e(m_1 + m_2)} = 558\text{V}. \quad (3.13)$$

If it is assumed that this voltage is reached instantaneously in the biased region, i.e. it is described by a step function, then, in the region where the potential is equal to U_0 , the collision energy is effectively zero and $\vec{v}_1 = \vec{v}_2$. The reaction may take place at any point within this interaction region, which only has the effect of varying the parameter L in equation 3.5. Outside this region, the voltage is zero, and the ions interact at higher collision energies (here, about 20 eV). The relative beam velocities of the ions is such that any MN events happening in these regions would end up outside the 200 ns detection window, and can therefore be ignored. Figure 3.3 plots the results of a simulation of the r distributions for the four channels in equation 3.11, assuming that only the second drift tube is biased ($L \sim 1.85\text{m}$).

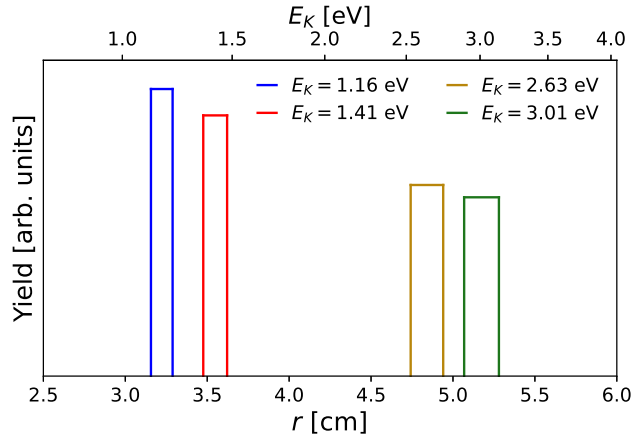


Figure 3.3: Simulation of the r distributions for the four channels in the MN of O^+ with O^- (given in equation 3.11, and assuming an ideal voltage potential).

Since events which occur at different points in this interaction region have different flight times, the separation r varies for events with the same kinetic energy release E_K , and one obtains a box-function distribution, as seen in the figure. Each box then corresponds to a specific kinetic energy release channel. The expected widths of these distributions can be simply evaluated from equation 3.5 as:

$$\Delta r = \sqrt{\frac{2E}{\mu} \frac{\Delta L}{v}}, \quad (3.14)$$

where ΔL is the length of the biased interaction region. Therefore, this broadening is larger for more energetic channels due to the square root dependence on the energy, which is noticeable in the spectrum here. The resolution is then only determined by this factor, and a maximum resolution would be obtained for a minimum-length interaction drift tube.

In reality, however, the applied bias voltage does not rise instantaneously. Minimising the interaction length has also the effect of worsening the profile of the voltage potential. This can be shown by simulating this potential based on the known size and geometry of the drift tubes, using the SIMION simulation software[61]. Figure 3.4 shows the result of such a simulation of this potential with a maximum at U_0 .

It then becomes clear that there are non-negligible regions of the interaction region in which the potential felt by the ions differs from the applied voltage. Consequently, the relative velocities Δv of the two ions is non zero over a significant fraction of the interaction region. This is illustrated on the right-hand axis of the figure, which shows that the relative velocity of the two ion beams varies between 0 and 22 km/s depending on at which point in the drift tube the interaction takes place. One must therefore evaluate the effects of this on final velocity components in order to correctly evaluate the resulting r distributions. A detailed derivation of this is found elsewhere [62], and the resulting vectors are given as:

$$\vec{u}_{\text{axial } 1} = \frac{\cos \gamma}{m_1} \left(\mu \cos \gamma \Delta v + \sqrt{(\mu \cos \gamma \Delta v)^2 + 2\mu E} \right) \quad (3.15)$$

$$\vec{u}_{\text{radial } 1} = \frac{\sin \gamma}{m_1} \left(\mu \cos \gamma \Delta v + \sqrt{(\mu \cos \gamma \Delta v)^2 + 2\mu E} \right). \quad (3.16)$$

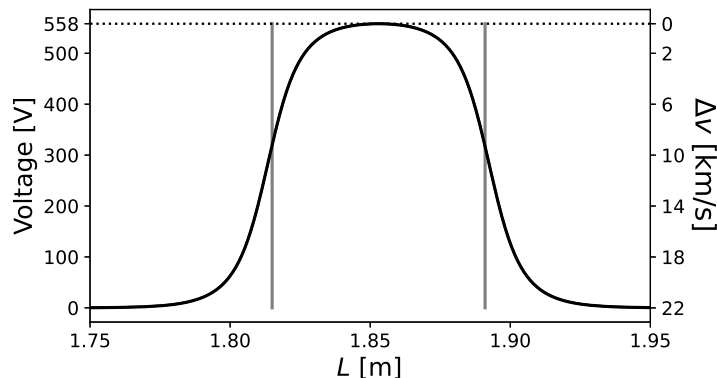


Figure 3.4: (a) Simulation of a realistic voltage potential on drift tube number 2, as a function of the distance L from the detector. The gray lines denotes the physical limits of the tube.

Similar expressions are derived for \vec{u}_2 . Setting $\Delta v = 0$, the previously derived equations 3.8 and 3.9 are retrieved. Note that only the difference in the axial velocity of the two ion beams is considered since the angle between the two beams is generally small (on the order of a few mrad).

In the region where the voltage differs from U_0 , the ions effectively interact with a higher collision energy. The expected effect on the distributions would therefore be the presence of “tails” on the distributions, extending to larger r . These tails, generally referred to as fringe field effects, are partially limited by the previously mentioned 200 ns time window. A related effect that is also important to consider in the simulation is that the MN cross section depends on the collision energy. As such, the probability for a MN event to take place somewhere along the interaction region will depend on the cross section at that specific collision energy. This generally depends on the studied system. However, for atomic systems, a model which well describes this dependence is known for low collision energies [63]:

$$\sigma \approx \pi R_x^2 \left(1 + \frac{1}{R_x E_{c.m.}} \right) \quad (3.17)$$

where R_x is the internuclear separation at which the electron transfer reaction takes place, and $E_{c.m.}$ is the collision energy. It follows that the reaction rate, k , has the relation:

$$k \propto \frac{1}{\sqrt{E_{c.m.}}} \quad (3.18)$$

In order to take this into account in the simulation, a reaction probability distribution at each point of the biased region is made based on equation 3.18. MN events are then generated randomly from this distribution using the Monte Carlo method. The result of such a simulation is shown in Figure 3.5.

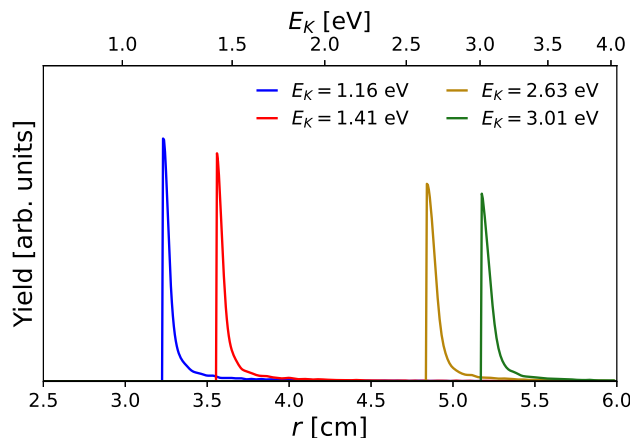


Figure 3.5: Simulation of the r distributions, assuming the voltage potential presented in Figure 3.4

Due to the MN rate dependence on the collision energy, sharper peaks are obtained, since the majority of events occur at the center of the potential rather than being equally distributed along the whole biased region. However, the previously mentioned fringe fields effects, i.e the tails to larger separations, result in an overlap between the distributions which can be problematic. One way to overcome this, is to look into the angular distribution of the events. If θ is defined as the angle between r and the beam axis, then it follows that:

$$\cos \theta = \frac{|v\Delta t|}{r} \quad (3.19)$$

At 0 eV collision energy, this quantity approximates to $\cos \gamma$ (previously defined in Figure 3.2), and, as a consequence, $\cos \theta$ should also be uniformly distributed. Events resulting from the fringe fields are, however, expected to mostly be distributed with $\cos \theta$ values close to 1, since the Δt term is then expected to dominate due to the large difference in the beam velocity Δv . The fringe field effects can therefore be limited by making an appropriate cut in the $\cos \theta$ distribution, a solution which was later adopted in Paper II.

There are other contributions to the experimental resolution which haven't been discussed so far. These include the energy spread of the ion beams, and the spread in the transverse velocity of the ions. The energy spread of the beam results in a decreased energy resolution [64], according to :

$$(\delta E_K)_{\delta E_i} = 2\sqrt{\frac{\mu E_K}{m_1 + m_2}} \left(\frac{\delta E_1 + \delta E_2}{\sqrt{(E_1 + E_2)}} \right), \quad (3.20)$$

where E_1 , E_2 are the beam energies, and δE_1 , δE_2 the corresponding energy spread. Whereas the angular spread $\delta\alpha$ results in an energy spread given by:

$$(\delta E)_{\delta\alpha} = \frac{\mu(E_1 + E_2)}{m_1 + m_2} (\delta\alpha)^2. \quad (3.21)$$

In addition, the spatial and timing resolution of the detection may also introduce their own broadening effects on the experimental distributions. While all these parameters can potentially be implemented into the simulation, they are often difficult to determine accurately. However, it is found that these broadening effects essentially scale with the square root of the of the kinetic energy release E_K , and the corresponding spread in the separation r is therefore expected to be the same for each channel. This broadening can therefore be simply modelled by a Gaussian function with an appropriate width. The final distributions are thus obtained by convolving the simulated distributions with this Gaussian using a width obtained from the observed experimental broadening. The result of such a simulation, fitted to an experimental spectra, is shown in Figure 3.6. A good agreement between the two are observed for all the peaks, except for a small (but significant) mismatch at around 5 cm, which is the subject of Paper I, discussed later.

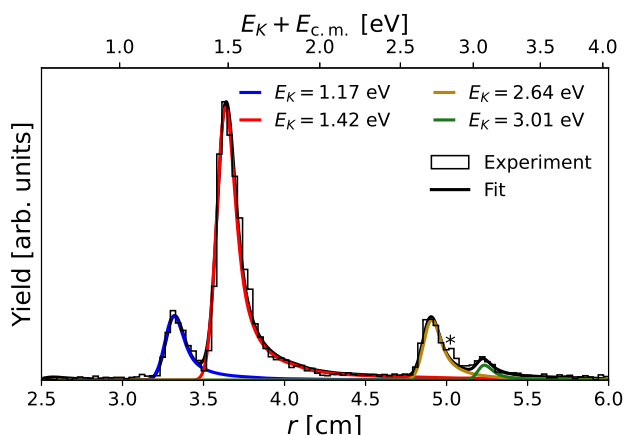


Figure 3.6: Simulated r distributions after convolution with a Gaussian, fitted to experimental data.

3.4 Three particle imaging

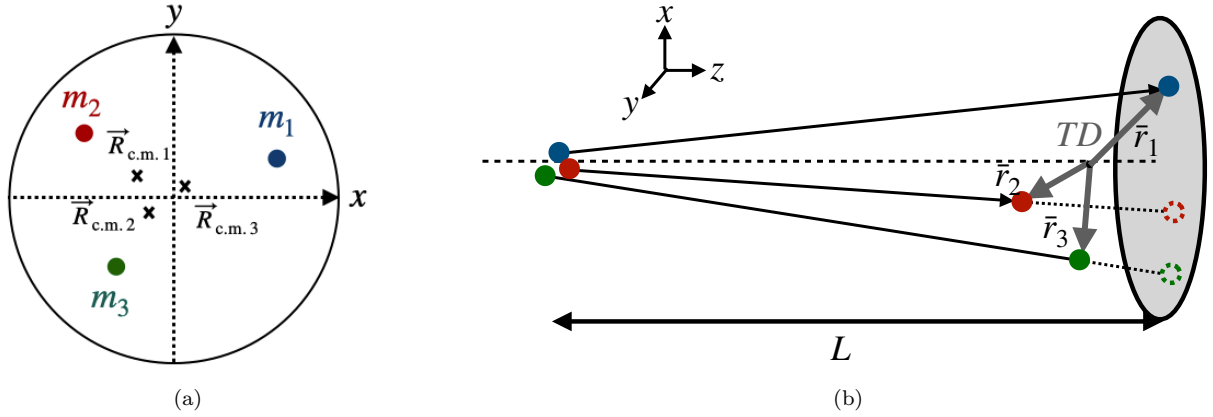


Figure 3.7: (a) Schematic of the center-of-mass selection described in the text (b) Schematic of the measured quantities for three particles

In the case of three products, the data evaluation is more complicated. To reconstruct the energy, one must first identify each particle. To achieve this, the center of mass in the x-y plane is first determined from the measured impact positions:

$$\vec{R}_{\text{CM}} = \frac{1}{\sum_{i=1}^3 m_i} \left(\sum_{i=1}^3 m_i \Delta x_i, \sum_{i=1}^3 m_i \Delta y_i \right). \quad (3.22)$$

If the particles have different masses, this must be calculated for each possible permutation and a selection is then made based on the axis of the center of mass of the overlapping ion-beams. An example of this is shown in Figure 3.7(a). Here, for simplicity, m_2 is chosen to be equal to m_3 , such that there are only three different combinations possible. The assumed correct permutation is obtained for $\vec{R}_{\text{CM}3}$, which lies closest to the center of the detector. This then allows to determine a specific “center-of-mass time”, in order to evaluate the third dimensional component. As in the two particle case, this corresponds to $v\Delta t_i$. However, here Δt_i is instead the time difference relative to the arrival time of the center-of-mass. The energy is then obtained by:

$$E \approx \frac{v^2}{2L^2} [m_1 \vec{r}_1^2 + m_2 \vec{r}_2^2 + m_3 \vec{r}_3^2], \quad (3.23)$$

where \vec{r}_i are the measured displacements, in position and time, from the selected center of mass. It is now possible to define a measurable quantity, equivalent to r in the two particle case, called the total displacement, TD , which is given by:

$$TD \equiv \sqrt{\frac{1}{M} \sum m_i \vec{r}_i^2} \approx \sqrt{\frac{2E}{M}} \frac{L}{v}. \quad (3.24)$$

A representation of this quantity is shown in Figure 3.7(b). The center point of three vectors correspond to the evaluated center of mass in position and arrival time differences of the three particles. The sum of these three vectors squared is proportional to the kinetic energy released. Note that here also the projected distances are used as an approximation of the two dimensional components.

3.5 Three particle simulation

The derivation of the final velocity vectors for three products is slightly more complex, due to the fact that energy and momentum conservation allows for many more possible geometries than in the two-product cases. The fraction of the energy that each particle carry can be described by two parameters a and b according to:

$$E_1 = aE, \quad E_2 = bE, \quad E_3 = (1 - a - b)E \quad (3.25)$$

The momenta vectors can always be described to lie in an arbitrary plane, and one can defines these as [65]

$$\vec{p}_1 = (p_{1x}, 0, 0), \quad \vec{p}_2 = (p_{2x}, p_y, 0), \quad \vec{p}_3 = (-(p_{1x} - p_{2x}), -p_y, 0) \quad (3.26)$$

where p_{1x} , p_{2x} and p_y can be defined from energy conservation. To the best of knowledge, these have only been derived for the cases with two or three particles of equal masses. For three particles of different masses, one obtains:

$$p_{1x} = \sqrt{2aEm_1}, \quad p_{2x} = \frac{(1-a-b)Em_3 - bEm_2 - aEm_1}{p_{1x}}, \quad p_y = \sqrt{2m_2bE - p_{2x}^2} \quad (3.27)$$

Due to momentum conservation, the parameters a and b are constrained. These can be derived from the possible extreme break-up scenarios. For example, the maximum value of a is obtained when $p_y = 0$, i.e. when the particles fragment with a completely linear geometry. Therefore, the limits of a are given by:

$$0 \leq a \leq \frac{m_2 + m_3}{m_1 + m_2 + m_3} \quad (3.28)$$

The second parameter b is constrained by a . For example, if a is zero, i.e., the first particle doesn't take up any energy, then the two other products must share all the energy as in a two-particle break-up. These limits are determined as:

$$b_{\text{lim}} = \frac{(1-a)(m_3^2 + m_2m_3) + a(m_1m_2 - m_1m_3) \mp 2\sqrt{am_1m_2m_3((1-a)(m_2 + m_3) - am_1)}}{(m_2 + m_3)^2} \quad (3.29)$$

where the minus/plus sign corresponds to the minimum and maximum value allowed respectively. For three particles of equal masses, these two equations simplify to:

$$0 \leq a \leq \frac{2}{3}, \quad \frac{1}{2} \left(1 - a - \sqrt{2a - 3a^2} \right) \leq b \leq \left(1 - a + \sqrt{2a - 3a^2} \right) \quad (3.30)$$

This allows to obtain a random distribution of the fraction of energies, as long as the parameters a and b are randomly interchanged between the three particles. Each of these combinations then correspond to different geometries, determined by the momentum vectors given in equations 3.26 and 3.27.

However, since the reaction can take place in a plane with any orientation in space, the vectors in the plane must be rotated randomly along both axis in order to cover all the Euclidean space. This is achieved by the means of Euler transformations, using the rotation matrices:

$$R_z = \begin{bmatrix} \cos \beta & -\sin \beta & 0 \\ \sin \beta & \cos \beta & 0 \\ 0 & 0 & 1 \end{bmatrix}, \quad R_y = \begin{bmatrix} \cos \psi & 0 & \sin \psi \\ 0 & 1 & 0 \\ -\sin \psi & 0 & \cos \psi \end{bmatrix}, \quad R_x = \begin{bmatrix} 1 & 0 & 0 \\ 0 & \cos \phi & -\sin \phi \\ 0 & \sin \phi & \cos \phi \end{bmatrix} \quad (3.31)$$

The first matrix R_z rotates the chosen x-y plane about the z-axis by the angle β , while the matrices R_y and R_x rotates the planes along the newly defined x-y axis, by the angles ψ and ϕ respectively. Here again $\cos \beta$ is uniformly distributed between -1 and 1 in order to maintain spherical symmetry.

From these velocity vectors, one can then compute the displacements of the three products in the detection system and compute the previously defined quantity TD (equation 3.24). Similarly as in the two particles cases, the resulting distributions are then convoluted with Gaussians of widths σ , determined from the observed experimental broadening.

3.6 Branching ratios

In order to extract the branching ratios into the different channels, two factors must first be determined: the collision energy, $E_{c.m}$, and the broadening factor, σ . In the case of an atomic system, the total energy is given by

$$E = E_K + E_{c.m} \quad (3.32)$$

where E_K is the kinetic energy release of the reaction. This value can directly determined from the energetics of the reaction and is therefore well known. The center-of-mass collision energy $E_{c.m}$ results in a small shift of the r distributions to larger separations, which can be included in the simulation as a free parameter. Similarly, the broadening factor σ can be extracted from the experimental data based on the observed

broadening. The resulting spectrum is therefore a linear combinations of the r distributions of each individual channel, i.e.

$$P(r, E_{c.m.}, \sigma) = \sum_i c_i p_i(r, E_{c.m.}, \sigma) \quad (3.33)$$

where c_i are the coefficients, i.e., the branching ratios, and p_i the simulated distributions. By fitting the data to the p_i functions, the branching ratios can thus be extracted.

While the statistical uncertainties of the fit itself are generally small, the coefficients are, on the other hand, highly sensitive to the parameters $E_{c.m.}$ and σ . The uncertainties are therefore rather calculated by varying these two parameters in the range where the fit is still viable. This way, the branching ratios are computed with error estimations which take into account the various uncertainties in the experiment.

As a last step of the analysis, the obtained values for the branching ratios are to be corrected for the angular acceptance of the detector system. In order to measure the arrival time differences of two particles, two different anodes in the multi-anode PMT must be triggered. This means that MN events in which the two products are mainly along the beam axis are less likely to be detected, as their separation in the detector plane are generally small. The detection efficiency can therefore be expressed in terms of the projected separation r_{\parallel} between the two neutrals on the detector. The horizontal plane of the detector and r_{\parallel} forms an angle ϕ as illustrated in Figure 3.8(a).

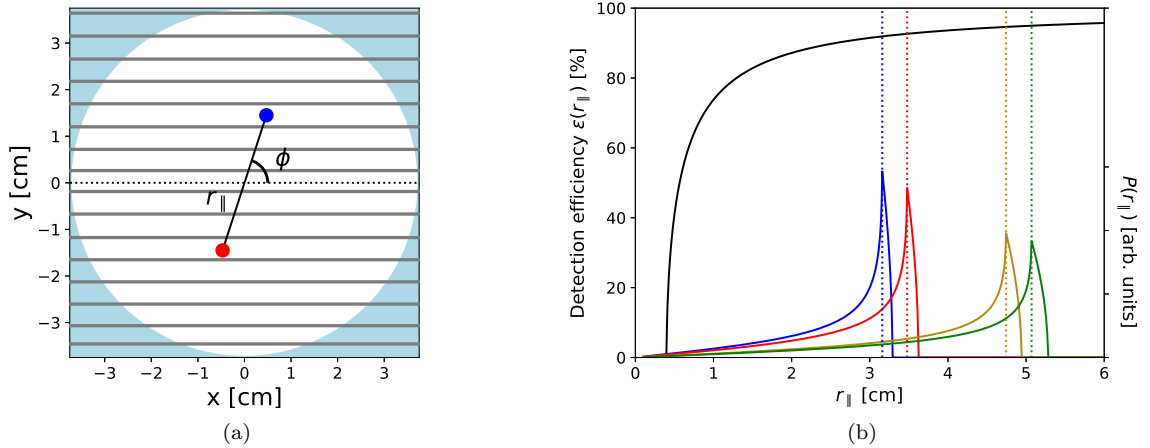


Figure 3.8: (a) Representation of two particles on the detection system. (b) Detection efficiency as a function of the projected distance r_{\parallel} (black line), in comparison with the simulated r_{\parallel} distributions for the four channels in equation 3.11.

The vertical separation of the two products can be related to this angle ϕ through:

$$\Delta y = r_{\parallel} \sin \phi \quad (3.34)$$

For two events to be detected, this separation should not be smaller than a certain value ($\Delta y_{\min} \sim 4\text{mm}$), and therefore the minimum angle is given by:

$$\phi_{\min} = \arcsin\left(\frac{\Delta y_{\min}}{r_{\parallel}}\right) \quad (3.35)$$

Summing over all possible angles ϕ yields the detection efficiency parameter ϵ as a function of the projected separation r_{\parallel} :

$$\epsilon(r_{\parallel}) = 1 - \frac{2 \arcsin(\Delta y_{\min}/r_{\parallel})}{\pi} \quad (3.36)$$

The detection efficiency for a given channel is then given by

$$\eta = \int_0^{r_{\parallel}^{\max}} \epsilon(r_{\parallel}) P(r_{\parallel}) dr_{\parallel} \quad (3.37)$$

where $P(r_{\parallel})$ is the probability distribution of r_{\parallel} . At low collision energies, the angular distribution can be considered to be isotropic, and $P(r_{\parallel})$ may be approximated as[66]

$$P(r_{\parallel}) = \frac{1}{r_{\parallel\max2} - r_{\parallel\max1}} \left(\arcsin \left(\frac{r_{\parallel}}{r_{\parallel\max1}} \right) - \arcsin \left(\frac{r_{\parallel}}{r_{\parallel\max2}} \right) \right) \quad (3.38)$$

where $r_{\parallel\max1}$ and $r_{\parallel\max2}$ correspond to the maximum values of the separations for events occurring at the limits of the interaction region. Figure 3.8(b) shows for example this detection efficiency factor $\epsilon(r_{\parallel})$ and the $P(r_{\parallel})$ distributions for the previously mentioned O^+/O^- system (equation 3.11).

It is found that the detection efficiency, plotted as the black curve in the figure, increases until it reaches a more or less constant level at around 90%. The efficiency is then only poor for events in which the separation is small, i.e below 1 cm. Furthermore, events for which the separation is smaller than 4 mm, can not be detected at all due to the width of the PMT's anodes. Fortunately, in an isotropic distribution, those events are rare, as shown by the coloured curves, representing the simulated distributions of the separations r_{\parallel} at 0 eV collision energy. Since this distribution is a projection of a sphere into a two dimensional detector, most events actually occur at large separations, which are detected in most cases. Therefore, the correction due to this effect is generally small.

However, another effect must be considered: A particle incident on the edge of a PMT strip may also trigger an adjacent channel, resulting in false two particle events. Since these events can not be distinguished from real MN events, a cutoff in the arrival time difference distribution ($\Delta t_{\text{cut}} = 5$ ns) is generally applied. This corresponds to a cut in the r_{\parallel} distribution according to:

$$r_{\parallel\text{cut}} = \sqrt{r_{\parallel\max}^2 - (v\Delta t_{\text{cut}})^2} \quad (3.39)$$

where $r_{\parallel\max}$ is the maximal separation for a given energy, which can be obtained from equation 3.5.

An additional detection efficiency term must therefore be implemented which results in a complicated analytical expression. An alternative solution is to instead use Monte Carlo simulations to calculate this detection efficiency. Rather than the projected separation r_{\parallel} , the angular distribution of $\cos\theta$ (equation 3.19) may be used, as it is expected to be uniform at low collision energies. One then obtains a detection efficiency map as a function of the kinetic energy release E_K of two products.

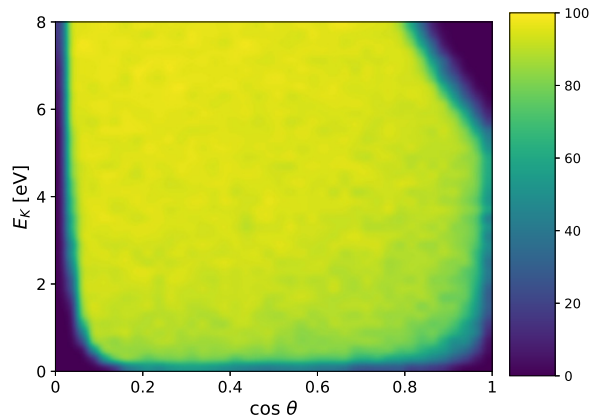


Figure 3.9: Simulated detection efficiency map for the $O^+ + O^-$ system

As seen in Figure 3.9, the detection efficiency mainly affects events with small or large $\cos\theta$ values. These correspond to events in which the time or spatial separation are small. In the 0-1 eV kinetic energy release range, this efficiency therefore increases gradually. At higher energies (>5 eV), the detection efficiency is found to decrease, which is instead due to the limited time window of the detection system, i.e the time separation starts exceeding 200 ns. The beam energies must therefore be chosen such that the channels to be investigated are in the region where the detection efficiency remains mainly the same, such that the corrections are negligible. There are, however, systems in which products covering a broad range of kinetic energies are observed, in which case the total detection efficiency may vary between the different product channels, as is the case for the iodine system discussed in Paper III.

For three particles, things are slightly more complex, as molecular ions are involved in the process. The collision energy $E_{c.m.}$ can not be determined accurately since the total energy is then given by:

$$E = E_K + E_{c.m} + E_{rot} + E_{vib} \quad (3.40)$$

where E_{rot} and E_{vib} are the initial vibrational and rotational energies of the parent molecular ions involved. Generally, these distributions are unknown and depend on the ion sources used, as well as the conditions in the source. The broadening and position of the distributions are still adjusted to match with the experimental data but more uncertainties are present due to the unknown magnitude of each contribution.

The corrections due to the detector efficiency are also difficult to evaluate. First, there do not exist any analytical functions describing the distributions of events on the detector and furthermore, these distributions are not necessarily isotropic, even at zero collision energy. This is because the final geometries of the three products depend on the fraction of energies a and b that the particles take, which depend on the break-up dynamics of the reaction. These must therefore be taken into account in the simulation.

3.7 Break-up dynamics

The energy sharing between three particles may be represented in a so called Dalitz-plot[67], as illustrated in Figure 3.10(a). The three particles have kinetic energies E_1 , E_2 and E_3 , where

$$E_1 + E_2 + E_3 = E \quad (3.41)$$

Here, the total energy E of the system might be represented in a triangle, in which the perpendiculars to the sides correspond to the magnitude of each of these kinetic energies. Therefore, each point inside the triangle correspond to a different energy sharing configuration. The center point correspond to an equal sharing of the energy, each segment corresponding to $1/3$ of the total energy. However, due to momentum conservation, not all configurations are physically allowed, as demonstrated in section 3.5. The allowed configurations determined by momentum conservation are described by the incircle of this triangle, as shown in the figure.

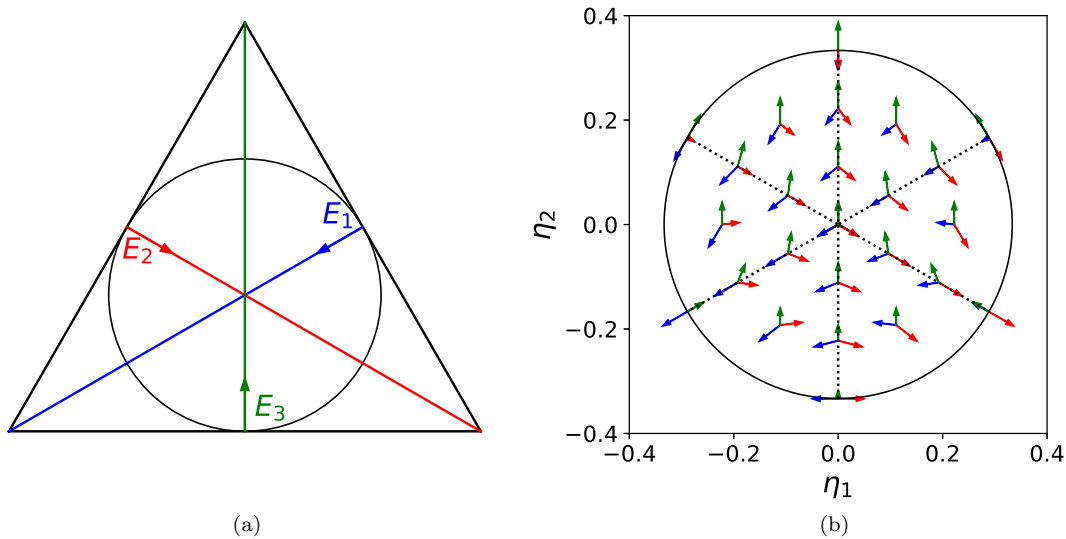


Figure 3.10: (a) Representation of energy and momentum conservation of three particles in a Dalitz plot (b) Representation of final geometries of three particles in a Dalitz plot.

In addition to yielding information about the energy sharing, Dalitz plots can be used to visualise the final geometry of the products. Each point inside the circle correspond to different values a and b in the energy sharing (see equations 3.25,3.26), which then correspond to different final velocity vectors. For three particles of equal mass, the coordinates of a given point inside this circle is given by:

$$\eta_1 = \frac{E_1 - E_2}{\sqrt{3}E}, \quad \eta_2 = \frac{2E_3 - E_2 - E_1}{3E}, \quad \eta_2 = \frac{2E_3 - E_2 - E_1}{3E} \quad (3.42)$$

Figure 3.10(b) shows a visual representation of some of these geometries. For example, when $\eta_1 = 0$, corresponding to the vertical line in the center, the energy sharing between particle 1 and 2 are equal, and the two resulting velocity vectors (blue and red arrows) are symmetric with respect to the third particle's vector (green arrow). The start and ends of those lines correspond to extreme case scenarios where linear geometries occur. These are generally the most interesting since these yield information about the break-up dynamics of the reaction. If two products are detected in close proximity, then they likely had vectors equal in magnitude and direction, which may indicate that the diatomic parent dissociated during the flight to the detector. This would suggest a sequential break-up in the reaction. On the other hand, if two products take up all the energy, i.e the third product is mostly found at the center, this could instead indicate that an intermediate highly excited state was formed.

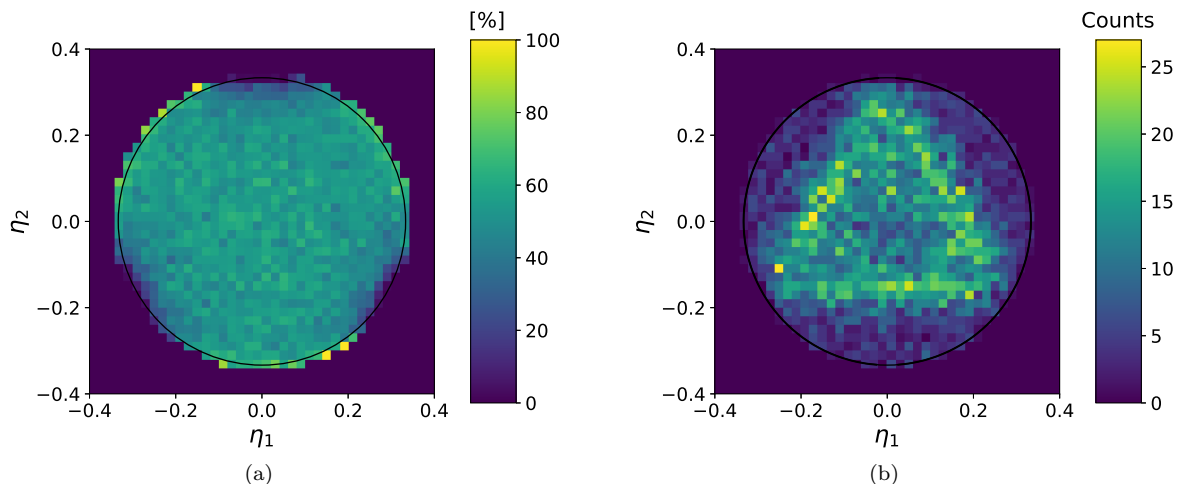


Figure 3.11: Dalitz plots of the $O(^3P)+O(^3P)+O(^3P)$ channel in the MN of O_2^+ with O^- . (a) Simulated uniform distribution (b) Experimentally retrieved distribution.

As an example, the Dalitz plots for the $O(^3P)+O(^3P)+O(^3P)$ channel in the MN of O_2^+ with O^- is shown in Figure 3.11. The left figure shows the simulated density distribution on the detector, assuming a uniform distribution of the energy sharing, while the right figure shows the experimentally retrieved distribution.

As can be seen, the simulated distribution is mostly uniform in the inside, while the contour varies largely. This is due to the related detection efficiency, as mentioned in the previous section. Similarly as for two particles, here the three products must hit three different PMTs in order to be detected. As such, the events in which two particles have similar vectors are less likely to be detected, resulting in the observed the three darker shadowed regions. The Dalitz plot can therefore be interpreted as a sort of detection efficiency map for three particles. One can thus see that this efficiency is much lower as for two particles, with most events having around 50-70% chance of being detected.

The experimentally retrieved distribution (Figure 3.11 shows a very different pattern, with a triangular structure inside of the circle where most counts are observed, while the rest of the Dalitz plot is mostly uniform. This triangle corresponds to mainly geometries in which two products are in proximity, which would therefore suggest a sequential break-up in O_2 . Since it is not possible to identify each oxygen atom, the structure is symmetric with respect to all three axis (see Figure 3.11(b)). The corrected Dalitz plot is then obtained by dividing the experimental plot with the detection efficiency map (not shown here).

4 Theoretical calculations

The theoretical calculations in Papers I, II, III were all performed by collaborators. The following section is therefore a short description of the methods used. For more details, see the indicated references.

4.1 Landau-Zener model

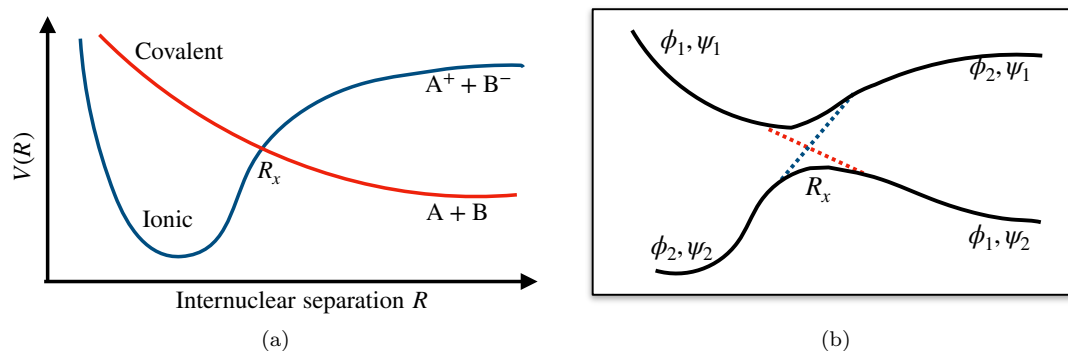


Figure 4.1: (a) Simplified sketch of the potential energy curves for the reactants and products in an MN reaction (b) Illustration of the diabatic/adiabatic trajectories in a two-level system.

In the case of an atomic system, the MN reaction can be described in terms of a single coordinate, namely the internuclear separation R . In a simplified model, one may consider two charged spheres approaching one another on this one dimensional potential energy curve. The ion pair $A^+ + B^-$ is described by a Coulombic attractive potential with a physical and nuclear repulsion at short separation. For the neutral pair $A+B$, there is no attraction, and so the minimum occurs at infinite separations. A sketch of such a system is shown in Figure 4.1(a). The two curves cross at a certain internuclear distance R_x , determined by the energetics of the system. This is where the reaction must take place since this is only the only point at which a transition from one system to the other is then possible.

In reality, the two systems are intrinsically connected. In order to determine the energy of a system at any particular point, one must mix the ionic and covalent wavefunctions. At the crossing point, the two states are degenerate and undistinguishable, and the energies of the true wavefunctions ψ_1 and ψ_2 are split apart, resulting in a region with an avoided crossing, as shown in Figure 4.1(b). Evaluating these wavefunctions in this region turns out to be a difficult task, since the Born Oppenheimer approximation is then no longer valid, which means one must evaluate the derivative terms in the Schrödinger equation. One way to solve this, is to introduce a diabatic basis in which the two curves do cross, i.e., the two states now are described by ϕ_1 and ϕ_2 in the figure. However, this results in the two states being coupled by the non diagonal elements H_{if} in the electronic Hamiltonian.

In 1932, Landau and Zener[20, 21] showed that the transition probability between the two systems can be related to this electronic coupling. The basic assumptions are that the diabatic potentials ϕ_1 and ϕ_2 vary linearly with R in the narrow region around the crossing point, and that the radial velocity $v_R = \frac{dR}{dt}$ can be described classically, i.e. :

$$E_{c.m.} - V_i(R) = \frac{\mu v_R^2}{2}, \quad (4.1)$$

where $E_{c.m.}$ is the collision energy, and V_i is the ionic pair potential, which is generally approximated as a $1/R$ Coulombic potential in the crossing region. However, since the collision may not always occur head-on, there is also an associated rotational energy barrier, and V_i may be written as:

$$V_i(R) = \frac{1}{R} + \frac{l(l+1)}{2\mu R^2} \quad (4.2)$$

The probability p to stay on the diabatic potential curve when passing the crossing point is then given by:

$$p = \exp\left(\frac{-2\pi H_{if}^2}{v_R |d(V_i - V_f)/dR|_{R=R_x}}\right) \quad (4.3)$$

where V_{\ddagger} is the diabatic covalent potential.

As the system passes the crossing point, there is a probability $1 - p$ that it transits to the covalent curve, and a probability p that it stays on this same curve on its way back. But there is also a probability p of staying on the ionic curve on its way in and a probability $1 - p$ to transit to the covalent curve on its way back. As such the total transition probability is given by:

$$P = 2p(1 - p), \quad (4.4)$$

When there are multiple channels, one must then consider all possible pathways for each channel. A general transition probability formula for N channels is given by [68]

$$P_j = (p_2 p_3 \dots p_j)(1 - p_j) \{1 + (p_{j+1} p_{j+2} \dots p_N)^2 + (1 - p_{j+2})^2 + [p_{j+1}(1 - p_{j+2})]^2 + [p_{j+1} p_{j+2}(1 - p_{j+3})]^2 + \dots + [p_{j+2} p_{j+2} \dots p_{N-1}(1 - p_N)]^2\}. \quad (4.5)$$

If there are several crossings present, the channels at short internuclear separations thus become less accessible due to the prior crossings at larger separations occurring first. The partial cross section for each channel is then obtained by summing over all these transition probabilities for each allowed value for the angular momentum l of the system.

$$\sigma_j = \frac{\pi}{2\mu E_{\text{c.m.}}} \sum_l (2l + 1) P_j(l) \quad (4.6)$$

The main difficulty in these calculations is to evaluate the coupling elements H_{if} . Generally, this coupling strength depends on the crossing point R_x and the ionization energies and electron affinities of the two atoms considered. Although several semi empirical formulas exist which estimate H_{if} to some degree of accuracy, these generally fail to take into account the effects of the angular momentum of the electrons. One model which effectively does this is the asymptotic centered anion model (ACAM).

4.2 Asymptotic centered anion model

The charge transfer between atoms A and B may be described as the motion of a single electron in a $A^+ + B + e^-$ system. Under the independent electron approximation, the Hamiltonian then becomes:

$$\hat{H} = -\frac{1}{2} \vec{\nabla}^2 + V_A(\vec{r}_A) + V_B(\vec{r}_B) \quad (4.7)$$

where $V_A(\vec{r}_A)$ and $V_B(\vec{r}_B)$ are the effective core potentials, and \vec{r}_A and \vec{r}_B are position vectors of the electron with respect to the center of cores A and B. Solving for the eigenvalues of this Hamiltonian, one obtains multiple expressions of integrals over the atomic wavefunctions ψ_A and ψ_B . One particular term, namely the exchange interaction $\Delta(R)$, relates to the delocalized part of the electronic distribution, and can be expressed as a surface integral[69]:

$$\Delta(R) = \int_S (\psi_B^*(\vec{r}_B) \nabla \psi_A(\vec{r}_A) - \psi_A^*(\vec{r}_A) \nabla \psi_B(\vec{r}_B)) d\vec{S} \quad (4.8)$$

where S is a sphere surface centered on atom B, with surface element $d\vec{S}$ directed inward. It can be shown[70] that, at the crossing point, this function approximates the coupling elements H_{if} in the diabatic basis:

$$H_{if} \approx \Delta(R_x)/2. \quad (4.9)$$

To evaluate this, one needs the atomic wavefunctions ψ_A and ψ_B on the sphere surface S . The basic assumption in the ACAM model is that since MN takes place at large internuclear separations, the asymptotic form of the anion's wavefunction ψ_B may be used, whereas ψ_A is given by the wavefunction of the active electron, centered on atom A (for more details see reference [71]). To derive these, the valence orbital in the electronic configuration of each atomic state is used. However, since the two approaching ions can form different molecular symmetries, these wavefunctions must be evaluated for each possible molecular state. These are determined from the Wigner-Witmer rules[72], from the atomic term symbols of the species of interest. As an example, Table 1 shows the possible molecular states which can be formed in the O^+/O^- system described earlier.

Atom pair	Λ	S	Molecular states
$O^+(^4S^o) + O^-(^2P^o)$	0,1	1,2	$^3,5\Sigma^-, ^3,5\Pi$
$O(3p\ ^3P) + O(^3P)$	0,1,2	0,1,2	$^1,3,5\Sigma^+(2), ^1,3,5\Sigma^-, ^1,3,5\Pi(2), ^1,3,5\Delta$
$O(3p\ ^5P) + O(^3P)$	0,1,2	1,2,3	$^3,5,7\Sigma^+(2), ^3,5,7\Sigma^-, ^3,5,7\Pi(2), ^3,5,7\Delta$
$O(3s\ ^3S^o) + O(^3P)$	0,1	0,1,2	$^1,3,5\Sigma^+, ^1,3,5\Pi$
$O(3s\ ^5S^o) + O(^3P)$	0,1	1,2,3	$^3,5,7\Sigma^+, ^3,5,7\Pi$

Table 1: Molecular states obtained from the Wigner-Witmer rules for the O^+/O^- system

Since the molecular symmetry and parity must be preserved, many of the listed states are not relevant to the reaction, such as the Δ states. The incoming ion pair can only form $^3,5\Sigma^-$ and $^3,5\Pi$ states, which are all present in the P+P pairs (row 2 and 3) but not in the S^o +P pairs (row 4,5), where the $^3,5\Sigma^-$ are absent. Therefore, the coupling to these states is zero for these two channels. The total cross section is obtained by evaluating the cross section for each molecular symmetry, and summing all of these while taking into account their statistical weight.

4.3 Multiconfigurational calculations

In the ACAM model, the independent particle approximation is used, which has the effect of partially neglecting the correlation in the motion of the electrons (note: some of the correlation is captured by the use of exact energies in the model). Atomic wavefunctions are then described by a single electronic configuration, and their orbital angular momentum L and their spin S . In reality, this label only designates the largest component, and, due to the electron correlated motion, each wavefunction is actually a mixture of configurations. One way to evaluate this is to perform MCHF (Multiconfigurational Hartree-Fock) calculations to determine the mixing components of each state. The method relies on the variational principle and the Hartree-Fock equations to determine the orbital functions, and the mixing coefficients are optimized by diagonalization of the Hamiltonian.

In MN, the captured electron generally ends up in an excited state of the formed neutral, and the final wavefunction ψ_f may then be described as combination of the cation core, A^+ , with an outer nl electron, i.e:

$$|\psi_f\rangle = |LS\rangle_{A^+} |nl\rangle \quad (4.10)$$

Due to configuration mixing, the wavefunction may also contain part of one (or more) excited states of the core configuration, i.e

$$|\psi_f\rangle = c_1 |L_1S_1\rangle |nl\rangle + c_2 |L_2S_2\rangle |nl\rangle \quad (4.11)$$

where c_1 and c_2 are parameters to be optimized in order to minimize the energy of the system. If the initial state ψ_i , is described by a $|L_1S_1\rangle$ core, then the second term may be neglected, and the coupling elements become

$$H_{if} = \langle\psi_i|\hat{H}|\psi_f\rangle = c_1 \langle\psi_i|\hat{H}|L_1S_1, nl\rangle \quad (4.12)$$

In Paper I and II, multiconfigurational Dirac-Hartree-Fock (MCDHF) calculations were employed through the GRASP2018 atomic structure code [73] to compute these coefficients in order to determine the coupling elements.

4.4 Ab initio calculations

The coupling elements H_{if} may also be evaluated directly, if the adiabatic potential energy curves known known. The quantity $\Delta(R_x)$ then corresponds to the difference in energies at the avoided crossing. In order to compute these energy curves *ab initio*, one must solve the time independent Schrödinger equation:

$$\hat{H}|\psi\rangle = E|\psi\rangle \quad (4.13)$$

For a molecular system, the total Hamilton operator \hat{H} is given by the sum of the kinetic (T) and electrostatic interactions (V) between the nuclei (N) and the electrons (e).

$$H_{\text{tot}} = T_N + T_e + V_{NN} + V_{Ne} + V_{ee} \quad (4.14)$$

The last term, corresponding to the electron-electron interaction, makes it impossible to solve the Schrödinger equation and is therefore generally captured by other means. The various computational methods available uses different type of approximations which provide different levels of accuracy.

In Paper III, the multi-reference configuration interaction (MRCI) method is used. The spatial correlation of the electrons is then captured by using linear combination of orbital configurations to describe the wave function of the system[74]. The electronic wave functions and associated potential energy curves are then calculated for each possible molecular symmetry, similarly as in the ACAM model.

5 Results

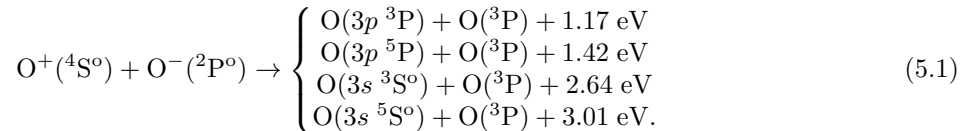
5.1 Paper I: Mutual neutralisation of O^+ with O^+

The mutual neutralisation of O^+ with O^- is one of the most important charge transfer reactions in the upper atmosphere. As highlighted in section 1.2, the excited oxygen atoms produced in these reactions result in ultraviolet equatorial airglow in our atmosphere, and the night-time ionospheric charge density depends largely on the rates and branching of this reaction.

It was first studied by Olson *et al.* in 1970[75], who measured the cross section in the 0.3-20 eV collision energy range, using a merged beam apparatus. Later, in 1989, Peart *et al.*[76] complemented these results by measuring the reaction over the 30-2000 eV range, this time using an inclined beams setup. However, a significant discrepancy was observed for the small gap of energy between the two experiments. This was eventually settled by Hayton & Peart[77] in 1993 with measurements over the 1-300 eV collision energy range in a novel merged-beam setup with a time-of-flight technique, and the discrepancy was attributed to space charge interactions present in the former setup of Olson *et al.*. It then took nearly 25 years before the reaction was studied once again. Using a state-of-the-art apparatus built at UCLouvain (Belgium), de Ruelle *et al.*[59] measured the cross section in the low collision energy range ($< 1\text{eV}$), completing the full range of energies. Using three dimensional imaging technique, they measured the product energy spectra, which allowed the determination of the branching ratios of the reaction for the first time.

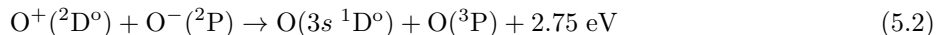
There was, however, a recurring source of uncertainty in all these experiments, namely the presence of metastable positive ions. In the experiment of de Ruelle *et al.*, these metastables manifested as additional features in the products energy spectra. As such, the reaction was a perfect test experiment for DESIREE: The results could be directly compared with those from de Ruelle *et al.*, and the storage capacities of DESIREE could potentially be used to eliminate eventual short-lived metastable species.

The available energy for excitation is given by the difference between the ionization energy of oxygen (13.62 eV[78]) and its electron affinity (1.46 eV[79]), which is 12.16 eV. Therefore, the reaction can in principle excite an oxygen atom up to the $3d$ states (~ 12.07 eV). However, as MN generally occurs at large inter-nuclear separations, the electron is found to be mainly captured into the $3p$ and $3s$ states, into the following four channels:



For the experiment at DESIREE, the O^+ beam was produced using the ECR source using molecular oxygen (O_2) whereas the O^- beam was produced from a TiO cathode in the SNICS source. The ions were accelerated to beam energies of 8.28 keV and 7.16 keV, respectively, and a scan of the drift-tube voltage was performed by evaluating the count rate as a function of the voltage applied to the drift tubes. A maximum in the count rate, and thus a minimum in the collision energy, was obtained at a voltage of ~ 570 V, which was then used during the data acquisitions. Note that this value differs from the calculated value (equation 3.13, $U_0 = 558$ V), since a slightly higher voltage must be applied to reach this value due to the shape of the potential. The interaction region was then limited to the second drift tube ($L \sim 1.85$ m), to yield the best resolution possible. Figure 5.1 shows the spectrum obtained, along with a fit of the simulated distributions, as explained in section 3.

The four channels of equation 5.1 were observed, with the $O(3p\ ^5P) + O(^3P)$ (red curve) found to dominate, in agreement with previous results of de Ruelle *et al.*. However, a small shoulder on the third peak was not accounted for in the simulation. Theoretical calculations using the Multichannel Landau Zener model combined with ACAM model were performed (see section 4.2 and 4.3), and the results showed that one channel from the first excited state of the cation, $O^+(^2D^o)$, had a significant cross section, namely:



This corresponded to the observed peak position in our spectra, and it was also found to coincide with an unassigned feature observed in the product energy spectra of de Ruelle *et al.*. This triggered a re-evaluation of the results by two of the co-authors A. Dochain and X. Urbain, and, after a thorough investigation, it was found that several small scale contributions in their spectra (not observed in the DESIREE spectra due to

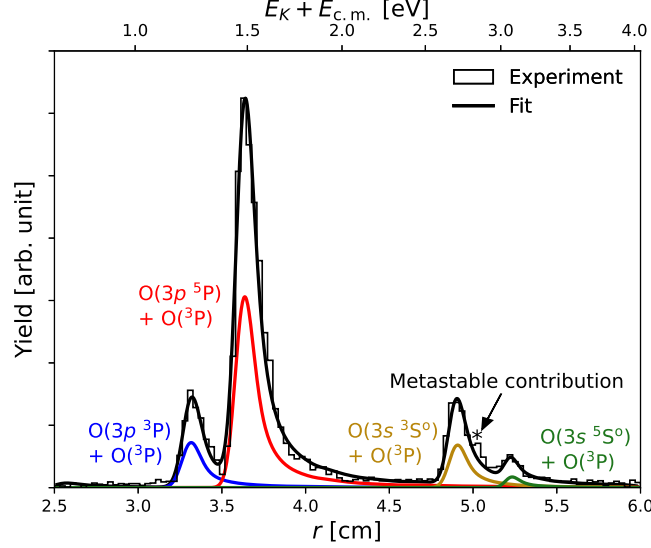
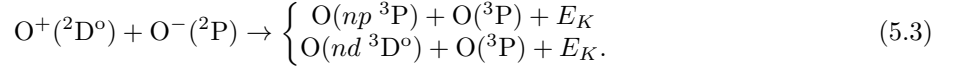


Figure 5.1: Yield of neutral O pairs as a function of the separation r between the products. The full curve results from a fit of the individual simulated distributions, shown in colored lines (reduced by a factor 2 for better visibility).

lower resolution and statistics) also corresponded to channels of this metastable state. Two Rydberg series were identified, namely:



These channels were not predicted by the theoretical model since these would require a spin flip in the core, a process which is forbidden. However, the transition could still potentially occur if those states had mixed configurations, something which is typically neglected in the ACAM model. As such, MCHF calculations were performed (see section 4.4) to determine the mixing content of the $\text{O}^+(^2\text{D}^\circ)$ cores in these states and the partial cross sections were computed for all those states.

Despite the inclusion of the mixing configuration, it was found that the theory was not in good agreement with the experimental observations in regard to these metastable contributions. The calculations predicted fairly small populations for the Rydberg series, while experimentally those were found to be present in non negligible amounts. This was particularly intriguing since the theoretical model used typically produces sensible results, specially when mixing configurational calculations are included [59, 80]. However, the calculations of the coupling elements in the ACAM model requires the evaluation of the Firsov integral (equation 4.8), for which certain criteria exist for its validity. It is for example required that the wavefunction of the active electron is exponentially decreasing in the integrated sphere. In other words, the overlap between the wavefunction of the active electron on the negative ion and the wavefunction of the active electron in the Rydberg state of the neutral, should be negligible in order for the model to work. This depends on where the crossing takes place, and in Janev & Salin's paper[69], the validity criterion is rather expressed as:

$$\gamma_2 R_x \gg 1 \quad (5.4)$$

where $\gamma_2 = \sqrt{2\text{EA}}$ (EA being the electron affinity of atom B). In the case of O^- , one therefore obtains:

$$R_x \gg 9.3 a_0 \quad (5.5)$$

Most of Rydberg states populated by the metastable cation were found to have crossings at lower or similar internuclear separations to this value, and the criterion is therefore not fulfilled. It was thus hypothesized that the observed discrepancy was due to this effect. However, in paper II, a different explanation for the discrepancy between theory and experiment is suggested.

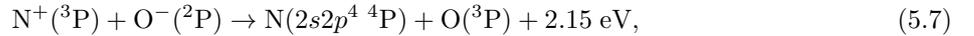
5.2 Paper II: Mutual neutralisation of N^+ with O^-

One other highly prevalent atomic ion in the upper atmosphere is of course nitrogen. Since the anion is unstable, mutual neutralisation may only occur between the nitrogen cation and the oxygen anion, i.e:



Since the relevance and applications of the reaction are very similar to the O^+/O^- reaction, the two systems have often been studied in conjunction in the past [76, 77]. In the recent aforementioned study of de Ruelle *et. al*[59], this particular system was also investigated, and the spectrum also showed significant contributions from metastable ions. Given the previous interesting findings in the MN of O^+ with O^- at DESIREE, and the theoretical challenges it represented, it was only natural to choose to study this system as well. The system also offered numerous kinetic energy release channels and would therefore allow to test the resolution limits of DESIREE.

Similarly as in the reaction with oxygen, the excess energy is sufficient to excite the captured electron in the $3s$ or $3p$ states of the neutral. However, there also exists a core-excited state in nitrogen into which the electron may be captured into:



which can only be described a single-electron process if the state is to be described a mixture of different configurations. In addition, there are two metastables states of N^+ which can potentially be ascribed to the observed additional features in the spectrum of de Ruelle *et. al*, $N^+(^1D)$, with a lifetime of $\approx 256\text{ s}$ [81] and $N^+(^1S)$, which has a lifetime of about 1 second. The latter could then be potentially be removed at DESIREE.

Beam energies of 7.00 keV were chosen for the two ions, in order to maximize the detection range and resolution. The N^+ ions were produced from N_2 gas introduced to the ECR ion source, and the O^- the same way as in the previous experiment. Other measures, such as optimisation and drift tube selection were made in the same way as in the previous experiment. However, additional measures were implemented both in the experiment and the analysis. Apertures were introduced at the entrance and exits of the merged section in order to improve the collimation of the ion beams, and a cut in the $\cos\theta$ distributions of the measured products was applied in order to limit the fringe fields effects, as explained in Section 3.3. As a result, the majority of the peaks could be individually resolved, as shown in Figure 5.2.

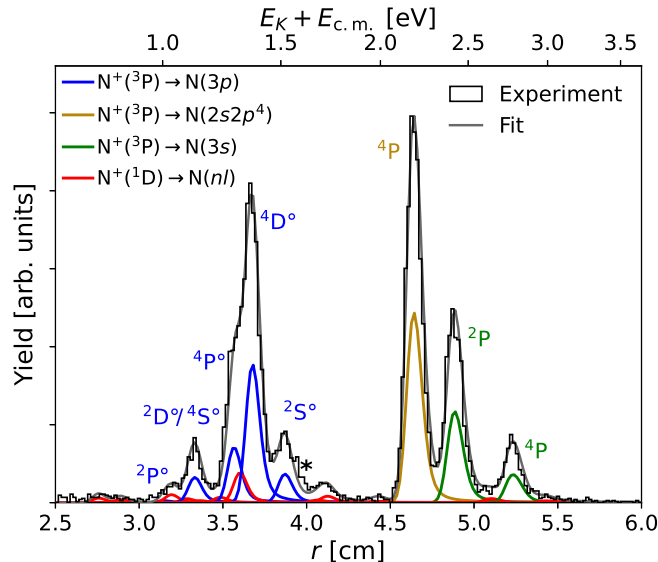


Figure 5.2: Yield of neutral N/O pairs as a function of the separation r between the products. The full curve results from a fit of the individual simulated distributions, shown in coloured lines (reduced by a factor 2 for better visibility).

As observed in the O^+/O^- system, the populations of the channels belonging to the ground state cation ($N^+(^3P)$) were found to be in good agreement between experiment and theory, while several observed contributions from the metastable cation ($N^+(^1D)$, shown in red in the figure) were not predicted

by our calculations. However, in contrast to the oxygen system, many states do fully satisfy the previously mentioned validity criterion of the theoretical model, which suggests that the discrepancy must arise from other factors. Furthermore, the highly mixed state $N(2s2p^4\ ^4P)$ (yellow curve) was well predicted by the calculations when configuration mixing was included, which suggests that the method used is indeed valid.

If one considers a state where the wavefunction is dominated by the ground state configuration, and we are interested in the metastable state's component, then it follows that:

$$H_{if} = c_1 \langle \psi(N^+(^1D)) | \hat{H} | \psi(N^+(^1D)nl) \rangle + c_2 \langle \psi(N^+(^1D)) | \hat{H} | \psi(N^+(^3P)nl) \rangle = c_1 \bar{H}_1 + c_2 \bar{H}_2 \quad (5.8)$$

The first term \bar{H}_1 corresponds to the one-electron process that we seek to evaluate, while the second term \bar{H}_2 is the two-electron process which the model can not evaluate, but we assume to be negligible. However this assumption is only valid if:

$$c_1 H_1 \gg c_2 H_2 \quad (5.9)$$

For many states of interest in both N and O, it was found that the mixing coefficient is of the order of 10^{-2} , which would then require:

$$\frac{H_1}{H_2} \gg 100. \quad (5.10)$$

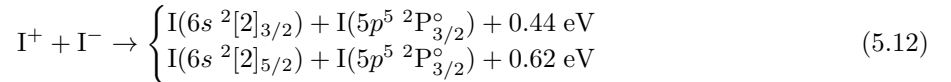
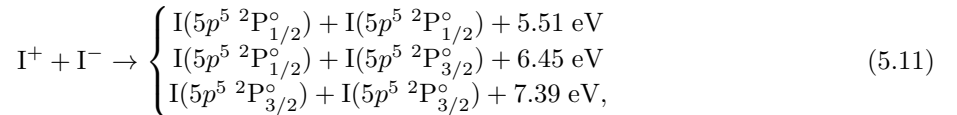
While coupling elements of multi-electron processes are generally small, it is not guaranteed that they are smaller by a factor 100 or more. Therefore, it is likely that the model can not predict these states correctly due to the presence of non-negligible multi-electron processes. This could also explain the observed discrepancy in Paper I, where several of the observed states are not well described by theory.

The results of the present paper also showed that a resolution close to the single-pass apparatus of UCLouvain could be achieved at DESIREE, when careful optimisation of the superimposition beams is undertaken. This was a particular milestone in the development of DESIREE, as one of the main purposes of the machine is to determine the branching ratios in MN reactions with accuracy. The two papers (Paper I and Paper II) show, however, that more advanced models are necessary to correctly describe the reaction, and in Paper III, *ab initio* methods are instead used to treat the reaction.

5.3 Paper III: Mutual neutralisation of I^+ with I^-

While iodine is present in the atmosphere due to the production of volatile species from algae in seawater, it rarely reaches high altitudes and therefore is mostly found in its neutral form [82]. The applications of the MN of iodine ions is therefore mainly of industrial use, more specifically, for electric plasma thrusters. Since these devices accelerate and eject ions to produce a propulsion, reactions involving ions in the plasma is likely to play a crucial role in the efficiency of such engines. In that regard, the data available are sparse and subject to high uncertainties, which makes iodine plasma modelling difficult. The two studies available on the reaction are over 50 years old and were both performed in afterglow plasmas in quite different experimental conditions compared to that found in an iodine thruster [83, 84]. Furthermore, the two studies provide no information on the nature of the products and there are uncertainties regarding the type of ions present (atomic/molecular). The system was therefore ideal to study at DESIREE, as the setup allows for ions to be mass-selected precisely and the products can be identified using the imaging detectors available. While absolute rates can not be determined at DESIREE, or at least not with precision, the product branching ratios are still of interest as they provide a direct test of theoretical models.

The system proved itself to be complex to investigate, both experimentally and theoretically. Due to the high electron affinity of iodine, and its lower ionisation potential, the MN reaction is not as energetically favorable as for the O^+/O^- and N^+/O^- systems (about 7.4 eV excess energy, compared to 12-13 eV). Consequently, only the ground state and the first excited state can be populated, i.e. :



For the ground state channel, equation 5.11, the kinetic energy release is quite high, which implies large separations of the products. Sufficiently high beam-energies must therefore be provided to ensure the products are captured by the detection system. On the other hand, for the channel with one iodine atom in the 6s excited state (equation 5.12), the kinetic energy is small, which is problematic as the detection efficiency decreases rapidly at small separations. Consequently, the system was studied at two different sets of beam energies. Using low beam energies (13 and 12 keV for the cation and anion respectively), the low energetic channels (equation 5.12) could be resolved in the spectrum. However, a large portion of the more energetic channels were found to fall outside the detection system. This can be visualised in Figure 5.3(a), which shows the simulated detection efficiency as a contour plot, together with the experimentally observed events. The data was therefore only used to determine the branching ratios between the two fine structure states.

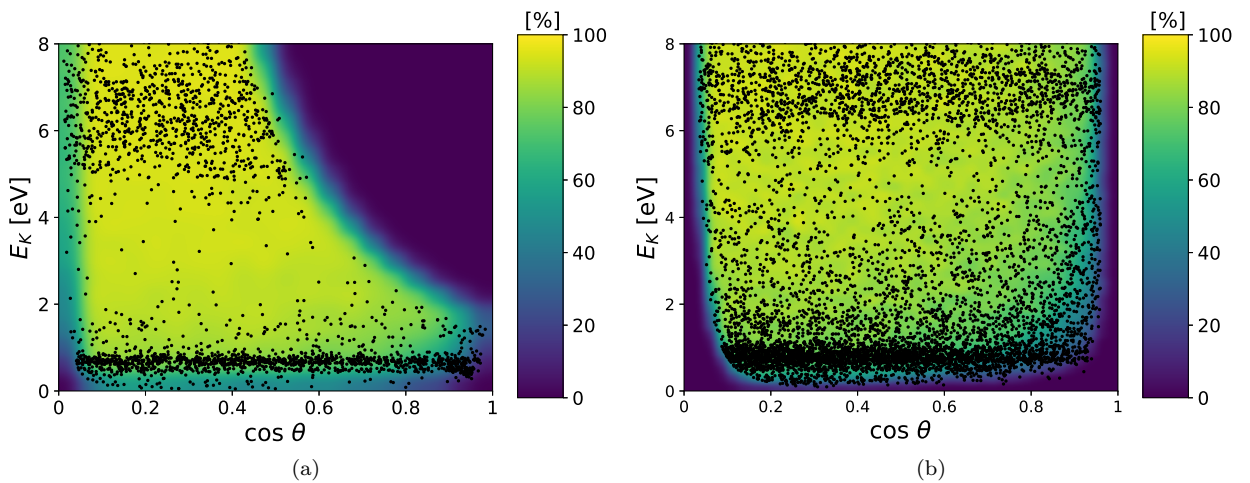


Figure 5.3: Detection efficiency maps as a function of the kinetic energy release E_K and $\cos \theta$ at (a) low beam energies and (b) high beam energies.

In the acquisition run at higher beam energies (35/30 keV), the more energetic channels are found to be detected equivalently, as highlighted in Figure 5.3(b). On the other hand, the low energetic channels are on the edge of the efficiency map and the counts distribution is found to vary as a function of $\cos\theta$. The corrections due to the channel detection efficiency therefore become important. However, the simulated detection efficiency map agrees well with the observed experimental distribution, and these corrections can be made rather accurately.

Theoretically, the system was also found to be a challenge, for mainly two reasons: Firstly, iodine is a heavy element, which means relativistic effects become important. Secondly, the avoided crossings for the low-energy channels (equation 5.12 take place at very short internuclear separations (about 3\AA), where simpler models are no longer valid. The system must therefore be treated with *ab initio* methods, as described in section 4.4. The results of these calculations showed complex potentials, with multiple avoided crossings in close proximity. The dynamics of the collisions were also computed and are to be the subject of a separate paper. Preliminary calculations indicate great agreement between the experimentally measured branching ratios and the theoretical ones.

5.4 Preliminary results: Mutual neutralisation of O_2^+ with O^-

As mentioned in the introduction, the upper layers of the atmospheres are exposed to high levels of radiation and are mostly composed of atomic ions, dominated by O^+ and N^+ . In lower layers however, less ionising radiation is present, due to the absorption from the F layer and the higher pressure, and molecular ions, such as O_2^+ , become prevalent.

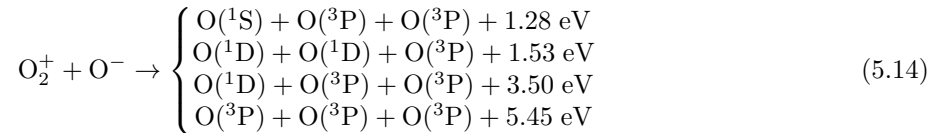
Destruction of O_2^+ typically occurs through dissociative recombination, a process which has been extensively studied both experimentally [85] and theoretically [16] in the past, due its importance to the green and red airglow in our atmosphere. However, very little is known about the corresponding mutual neutralisation reaction. Early measurements suggests that the cross section for the reaction is of the same order as for the atomic ions (Paper I), but no information on the nature and distribution of the final products exist.

In early recombination studies, it was found that triatomic systems predominantly formed two reaction products, with one being a molecule. For the MN of O_2^+ with O^- , this would be:



where the kinetic energy released, E_K , would depend on the electronic, rotational and vibrational state of the molecule. With 10.63 eV available in the reaction, a large number of product channels are then possible.

However, for the triatomic cation O_3^+ , it was found instead that the reaction was largely dominated by dissociation into three atoms [86]. A similar scenario can therefore be thought to occur for the MN of O_2^+ with O^- as well, as the excess energy is actually sufficient to open up four three-body channels:



To the best of our knowledge, there are no published results on break-up dynamics of MN reactions. There was therefore an additional strong motivation to study this system at DESIREE.

Given the large kinetic energy in the three body break-up, relatively high beam energies were selected (40 and 18 keV for the cation and anion beam respectively), and three drift tubes were chosen to be biased, as a compromise between resolution and count statistics. As expected, only the three-body break-up was actually observed. Figure 5.4(a) shows the spectrum obtained.

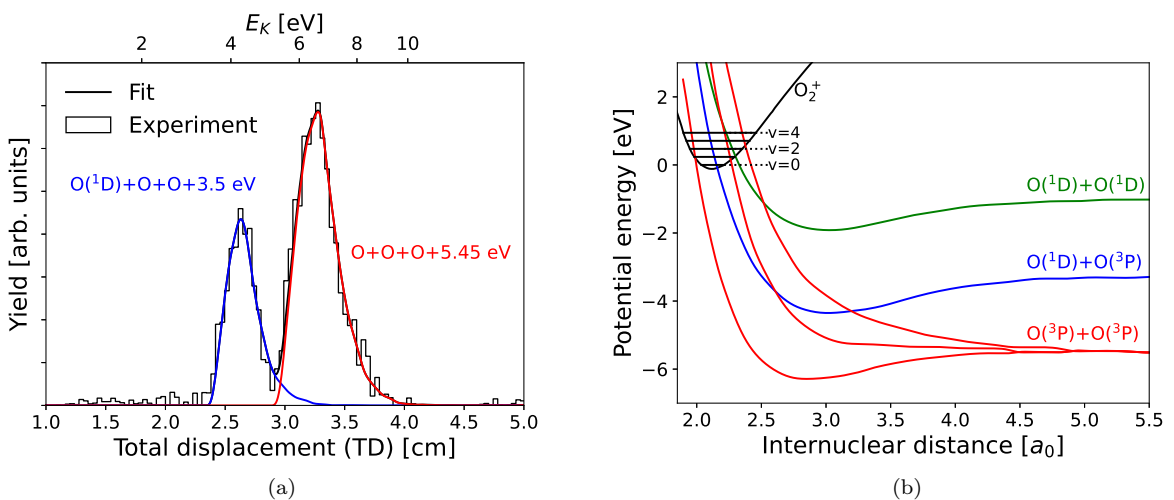


Figure 5.4: (a) Yield of neutral fragments as a function of their total displacement TD from their center of mass. The fit of the individual simulated distributions are shown in colored lines. (b) Potential energy curves relevant for the reaction.

However only two out of the four channels of equation 5.14 were actually observed, with a preference for the more energetic channel (red curve), where all three oxygen atoms end up in the ground state. This

was a strong contrast to the dissociative recombination results, which showed a high predilection for the formation of excited states of oxygen.

Theoretically, MN systems involving molecular ions are difficult to treat since they require evaluating the potential energy curves along the different reaction coordinates of the multinuclear system. In the absence of such calculations, we chose to understand the dynamics in a simplified model, in which the anion does not participate in any bonding, i.e., it is treated as an electron donor only. In this model, the O_2^+/O_2 potential energy curves may be used, with the neutral curves shifted by the electron affinity of O^- in order to take into account the energy required to transfer the electron from the anion.

Using this model, the results are particularly interesting (see Figure 5.4(b)). The $O(^3P)+O(^3P)$ channel has multiple dissociative states coupled to it (red curves), each of which cross the ionic potential (black curve) at different vibrational quanta in $O_2^+(v)$. On the other hand, the $O(^1D)+O(^3P)$ (blue curve) crosses the O_2^+ potential only at its lowest energy, $O_2^+(v=0)$. It is therefore possible that the higher proportion of ground states products observed is due to the presence of these additional crossings at higher vibrational states. As such, the branching ratios could depend on the vibrational state of the cation. Such effects can be expected, and have also been observed in the dissociative recombination of diatomic ions [87] However, this is a very simplified approach of the dynamics. For example, it doesn't explain the absence of the $O(^1D)+O(^1D)$ channel (green curve), which also has a favourable crossing with the ionic potential at around $O_2^+(v=1)$.

The Dalitz plots also reveal intriguing dynamics in the reaction. The lower energetic channel has larger density of events in three specific corners of the break-up dynamics map (see Figure 3.10(b)) which correspond to linear structures. In the higher energetic channel, the opposite is observed, no events are observed in these regions and furthermore, a very specific pattern is observed, namely a triangular shape within the Dalitz circle. This shape is obtained when one fragment gets a specific fraction of the energy frequently, while the rest of the kinetic energy is distributed randomly between the other fragments. In other words, the break-up was initially a two-body reaction, shortly followed by dissociation of the molecule, indicating a sequential break-up.

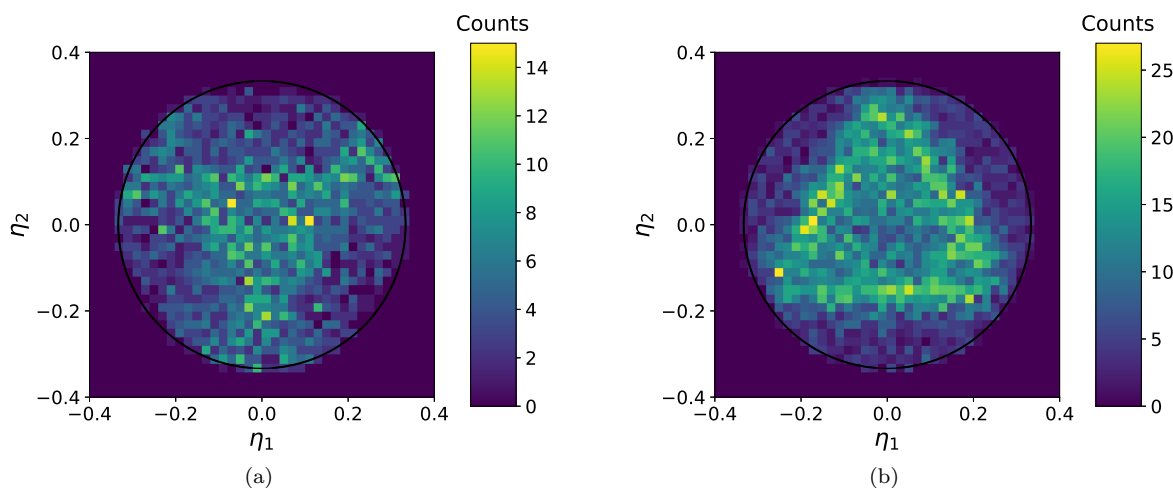


Figure 5.5: Dalitz plots of the (a) $O(^1D)+O(^3P)+O(^3P)$ channel (b) $O(^3P)+O(^3P)+O(^3P)$ channel

6 Conclusions and Outlook

The double electrostatic ion storage ring DESIREE is a unique facility aimed at studying mutual neutralisation of oppositely charged ions. It was fully commissioned in 2017, with the first merged beams results of MN reactions published in 2020 [38]. In the first phase of DESIREE, the conducted experiments have been mainly aimed at reproducing the pioneering works of Urbain *et al.* at the single-pass merged beam apparatus located in UCLouvain.

In Paper I and II, the atmospherically relevant O^+/O^- and N^+/O^- reactions were studied, and the experimental results were found to be in good agreement between the two setups. However, the presence of contributions from metastable ions raised questions and a collaboration with a theoretical group in Uppsala was initiated. It was found that the collision dynamics could be well described by the semi classical Landau Zener model combined with an asymptotic approach for the estimation of the couplings. While good agreement between and theory and experiment could be achieved for the reaction involving the ground state cation, the calculations had limited agreement with results involving the metastable state cation, and it was concluded that multi-electron processes might be present, which would require more advanced theoretical modelling.

In Paper III, a more complex reaction was selected, which hadn't been studied previously in any merged-beam apparatus, namely the ionic iodine collision system. The work was performed in collaboration with a theoretical group at Sorbonne Université, which seek to model the processes taking place in iodine electric thrusters. It was found that *ab initio* calculations were necessary to correctly describe the collision, as multiple avoided crossings at short internuclear separations were found to be present, which could explain the observed formation of ground state neutrals pairs.

Lately, experiments on more complex systems have been conducted, such as the one presented in the preliminary results, i.e the mutual neutralisation of a diatomic oxygen cation with an oxygen anion. The detection of three products from an MN reaction was thus observed for the first time, and the results were found to exhibit intriguing dynamics. However, the theoretical treatment of such reactions is very recent and it is still unknown which level of accuracy can be achieved.

Other preliminary results, not presented here, include NO^+ and N_2^+ , interacting with O^- , as well as I_2^+ with I^- . While NO^+ can cool down vibrationally, due to presence of an intrinsic dipole moment, the other mentioned homonuclear diatomic ions cannot. The goal of future studies is therefore to use isotopologues of these molecules in order to induce radiative transitions and study the system at lower quantum levels. This would for example allow to confirm or refute the possible vibrational dependance in the MN of O_2^+ with O^- . Other projects involve studying systems which are more relevant to cosmology, such as the MN of the first two ions in the universe, namely HeH^+ and H_2^+ with H^- .

References

- ¹E. W. McDaniel, *Collision phenomena in ionized gases* (Wiley, 1964).
- ²V. G. Anicich, “An index of the literature for bimolecular gas phase cation-molecule reaction kinetics”, JPL Publication (2003).
- ³G. P. Harnwell, “Angular scattering of electrons in helium, neon, hydrogen and nitrogen”, *Phys. Rev.* **33**, 559–571 (1929).
- ⁴M. J. Brunger and S. J. Buckman, “Electron–molecule scattering cross-sections. i. experimental techniques and data for diatomic molecules”, *Physics Reports* **357**, 215–458 (2002).
- ⁵H. S. W. Massey and D. R. Bates, *Rep. Prog. Phys.* **9**, 61 (1943).
- ⁶W. G. Graham, W. Frisch, Y. Hahn, and J. Tanis, *Recombination of atomic ions* (1992).
- ⁷A. Burgess, “Delectronic recombination and the temperature of the solar corona”, *Astrophysical Journal* **139**, 776–780.
- ⁸H. A. Kramers, “Xciii. on the theory of x-ray absorption and of the continuous x-ray spectrum”, *The London, Edinburgh, and Dublin Philosophical Magazine and Journal of Science* **46**, 836–871 (1923).
- ⁹I. A. Kotelnikov and A. I. Milstein, “Electron radiative recombination with a hydrogen-like ion”, *Physica Scripta* **94**, 055403 (2019).
- ¹⁰J. H. Scofield, “Angular and polarization correlations in photoionization and radiative recombination”, *Phys. Rev. A* **40**, 3054–3060 (1989).
- ¹¹M. Tokman, N. Eklöw, P. Glans, E. Lindroth, R. Schuch, G. Gwinner, D. Schwalm, A. Wolf, A. Hoffknecht, A. Müller, and S. Schippers, “Dielectronic recombination resonances in F^{6+} ”, *Phys. Rev. A* **66**, 012703 (2002).
- ¹²D. C. Griffin, “A review of radiative and dielectronic recombination for C and O ions”, *Physica Scripta* **T28**, 17–24 (1989).
- ¹³D. A. Verner and G. J. Ferland, “Atomic Data for Astrophysics. I. Radiative Recombination Rates for H-like, He-like, Li-like, and Na-like Ions over a Broad Range of Temperature”, *ApJS* **103**, 467 (1996).
- ¹⁴D. R. Bates, “Dissociative recombination”, *Phys. Rev.* **78**, 492–493 (1950).
- ¹⁵A. Petrigani, F. Hellberg, R. D. Thomas, M. Larsson, P. C. Cosby, and W. J. van der Zande, “Electron energy-dependent product state distributions in the dissociative recombination of O_2^+ ”, *Chem. Phys.* **122**, 234311 (2005).
- ¹⁶S. L. Guberman, “Mechanism for the green glow of the upper ionosphere”, *Science* **278**, 1276–1278 (1997).
- ¹⁷J.-H. Yee and T. Killeen, “Thermospheric production of $O(^1S)$ by dissociative recombination of vibrationally excited O_2^+ ”, *Planetary and Space Science* **34**, 1101–1107 (1986).
- ¹⁸V. Zhaunerchyk, A. Al-Khalili, R. D. Thomas, W. D. Geppert, V. Bednarska, A. Petrigani, A. Ehlerding, M. Hamberg, M. Larsson, S. Rosen, and W. J. van der Zande, “Rotational state effects in the dissociative recombination of H_2^+ ”, *Phys. Rev. Lett.* **99**, 013201 (2007).
- ¹⁹J. Brian and A. Mitchell, “The dissociative recombination of molecular ions”, *Physics Reports* **186**, 215–248 (1990).
- ²⁰L. Landau, “On the theory of transfer of energy at collisions ii”, *Phys. Z. Sowjetunion* **2**, 118 (1932).
- ²¹C. Zener and R. H. Fowler, “Non-adiabatic crossing of energy levels”, *Proc. Math. Phys. Eng. Sci.* **137**, 696–702 (1932).
- ²²E. Ferguson, F. Fehsenfeld, D. Dunkin, A. Schmeltekopf, and H. Schjff, “Laboratory studies of helium ion loss processes of interest in the ionosphere”, *Planetary and Space Science* **12**, 1169–1171 (1964).
- ²³D. Smith, N. G. Adams, A. G. Dean, and M. J. Church, “The application of langmuir probes to the study of flowing afterglow plasmas”, *J. Phys. D: Appl. Phys.* **8**, 141–152 (1975).
- ²⁴J. Deson, F. Haloua, C. Lalo, A. Rousseau, and V. Veniard, “Detection of H atoms in the flowing afterglow of a microwave plasma by multiphoton laser-induced fluorescence: atom-removal kinetics”, *J. Phys. D: Appl. Phys.* **27**, 2320–2328 (1994).
- ²⁵K. T. Dolder, *Case Studies in Atomic Collision Physics* (1969).
- ²⁶R. Y. Neymaber, *Methods of Experimental Physics* **7A** (1968).
- ²⁷J. T. Moseley, W. Aberth, and J. R. Peterson, *Phys. Rev. Lett.* **24**, 435–7 (1970).

- ²⁸R. D. Rundel, K. L. Aitken, and M. F. A. Harrison, *J. Phys. B: Atom. Mol. Phys.* **2**, 954 (1969).
- ²⁹T. D. Gaily and M. F. A. Harrison, *J. Phys. B: Atom. Mol. Phys.* **3**, L25–7 (1970).
- ³⁰S. Szucs, M. Karemera, M. Terao, and F. Brouillard, “Experimental study of the mutual neutralisation of H^+ and H^- between 5 and 2000 eV”, *J. Phys. B: At. Mol. Opt. Phys.* **17**, 1613–1622 (1984).
- ³¹B. Peart, M. A. Bennett, and K. Dolder, “New measurements of the mutual neutralisation of H^+/H^- and He^+/He^- ions”, *J. Phys. B: At. Mol. Opt. Phys.* **18**, L439–L444 (1985).
- ³²B. Peart and D. A. Hayton, “Merged beam measurements of mutual neutralization of H^+ and H^- ions”, *J. Phys. B: At. Mol. Opt. Phys.* **25**, 5109–5119 (1992).
- ³³P. Baumann, M. Blum, A. Friedrich, C. Geyer, M. Grieser, B. Holzer, E. Jaeschke, D. Krämer, C. Martin, K. Matl, R. Mayer, W. Ott, B. Povh, R. Repnow, M. Steck, E. Steffens, and W. Arnold, “The Heidelberg heavy ion test storage ring TSR”, *Nucl. Instrum. Methods Phys. Res. A: Accel. Spectrom. Detect. Assoc. Equip.* **268**, 531–537 (1988).
- ³⁴S. Moller, “ASTRID—a storage ring for ions and electrons”, in Conference record of the 1991 IEEE particle accelerator conference, Vol. 5 (1991), pp. 2811–2813.
- ³⁵K. Abrahamsson, G. Andler, L. Bagge, E. Beebe, P. Carlé, H. Danared, S. Egnell, K. Ehrnstén, M. Engström, C. Herrlander, J. Hilke, J. Jeansson, A. Källberg, S. Leontein, L. Liljeby, A. Nilsson, A. Paal, K.-G. Rensfelt, U. Rosengård, A. Simonsson, A. Soltan, J. Starker, M. Ugglas, and A. Filevich, “CRYRING — a synchrotron, cooler and storage ring”, *Nucl. Instrum. Methods Phys. Res. B: Beam Interact. Mater. At.* **79**, 269–272 (1993).
- ³⁶R. D. Thomas, H. T. Schmidt, G. Andler, M. Björkhage, M. Blom, L. Brännholm, E. Bäckström, H. Danared, S. Das, N. Haag, P. Halldén, F. Hellberg, A. I. S. Holm, H. A. B. Johansson, A. Källberg, G. Källersjö, M. Larsson, S. Leontein, L. Liljeby, P. Löfgren, B. Malm, S. Mannervik, M. Masuda, D. Misra, A. Orbán, A. Paál, P. Reinherd, K.-G. Rensfelt, S. Rosén, K. Schmidt, F. Seitz, A. Simonsson, J. Weimer, H. Zettergren, and H. Cederquist, “The double electrostatic ion ring experiment: a unique cryogenic electrostatic storage ring for merged ion-beams studies”, *Rev. Sci. Instrum.* **82**, 065112 (2011).
- ³⁷H. T. Schmidt, R. D. Thomas, M. Gatchell, S. Rosén, P. Reinherd, P. Löfgren, L. Brännholm, M. Blom, M. Björkhage, E. Bäckström, J. D. Alexander, S. Leontein, D. Hanstorp, H. Zettergren, L. Liljeby, A. Källberg, A. Simonsson, F. Hellberg, S. Mannervik, M. Larsson, W. D. Geppert, K. G. Rensfelt, H. Danared, A. Paál, M. Masuda, P. Halldén, G. Andler, M. H. Stockett, T. Chen, G. Källersjö, J. Weimer, K. Hansen, H. Hartman, and H. Cederquist, “First storage of ion beams in the double electrostatic ion-ring experiment: DESIREE”, *Rev. Sci. Instrum.* **84**, 055115 (2013).
- ³⁸G. Eklund, J. Grumer, S. Rosén, M. Ji, N. Punnakayathil, A. Källberg, A. Simonsson, R. D. Thomas, M. H. Stockett, P. Reinherd, P. Löfgren, M. Björkhage, M. Blom, P. S. Barklem, H. Cederquist, H. Zettergren, and H. T. Schmidt, “Cryogenic merged-ion-beam experiments in DESIREE: Final-state-resolved mutual neutralization of Li^+ and D^- ”, *Phys. Rev. A* **102**, 012823 (2020).
- ³⁹J. Qin, J. J. Makela, F. Kamalabadi, and R. R. Meier, “Radiative transfer modeling of the oi 135.6 nm emission in the nighttime ionosphere”, *J. Geophys. Res. Space Phys.* **120**, 10116–10135 (2015).
- ⁴⁰B. A. Tinsley, A. B. Christensen, J. Bittencourt, H. Gouveia, P. D. Angreji, and H. Takahashi, “Excitation of oxygen permitted line emissions in the tropical nightglow”, *J. Geophys. Res.* **78**, 1174–1186 (1973).
- ⁴¹R. P. Wayne, *Chemistry of atmospheres* (Clarendon Press, Oxford (UK), 1991).
- ⁴²J. L. Fox, “The production and escape of nitrogen atoms on Mars”, *J. Geophys. Res. Planets* **98**, 3297–3310 (1993).
- ⁴³M. B. McElroy, M. J. Prather, and J. M. Rodriguez, “Escape of hydrogen from Venus”, *Science* **215**, 1614–1615 (1982).
- ⁴⁴V. Vuitton, P. Lavvas, R. Yelle, M. Galand, A. Wellbrock, G. Lewis, A. Coates, and J.-E. Wahlund, “Negative ion chemistry in Titan’s upper atmosphere”, *Planetary and Space Science* **57**, 1558–1572 (2009).
- ⁴⁵A. Bogaerts and E. C. Neyts, “Plasma technology: an emerging technology for energy storage”, *ACS Energy Letters* **3**, 1013–1027 (2018).
- ⁴⁶S. Adams, J. Miles, and A. Laber, “Resonant laser induced breakdown for fuel-air ignition”, in 48th AIAA Aerospace sciences meeting (2010).
- ⁴⁷S. Williams, S. Popovic, L. Vuskovic, C. Carter, L. Jacobson, S. Kuo, D. Bivolaru, S. Corera, M. Kahan-dawala, and S. Sidhu, “Model and igniter development for plasma assisted combustion”, in 42nd AIAA Aerospace sciences meeting and exhibit (2004).

- ⁴⁸A. Ehlerding, F. Hellberg, R. Thomas, S. Kalhori, A. A. Viggiano, S. T. Arnold, M. Larsson, and M. af Ugglas, “Dissociative recombination of C_2H^+ and $C_2H_4^+$: Absolute cross sections and product branching ratios”, *Phys. Chem. Chem. Phys.* **6**, 949–954 (2004).
- ⁴⁹A. M. Derkach, A. Al-Khalili, L. Viktor, A. Neau, W. Shi, H. Danared, M. af Ugglas, and M. Larsson, “Branching ratios in dissociative recombination of the $C_2H_2^+$ molecular ion”, *J. Phys. B: At. Mol. Opt. Phys.* **32**, 3391–3398 (1999).
- ⁵⁰P. Grondein, T. Laffleur, P. Chabert, and A. Aanesland, “Global model of an iodine gridded plasma thruster”, *Physics of Plasmas* **23**, 033514 (2016).
- ⁵¹D. Levko and L. L. Raja, “Fluid modeling of inductively coupled iodine plasma for electric propulsion conditions”, *Journal of Applied Physics* **130**, 173302 (2021).
- ⁵²H. T. Schmidt, G. Eklund, K. C. Chartkunchand, E. K. Anderson, M. Kamińska, N. de Ruelle, R. D. Thomas, M. K. Kristiansson, M. Gatchell, P. Reinhed, S. Rosén, A. Simonsson, A. Källberg, P. Löfgren, S. Mannervik, H. Zettergren, and H. Cederquist, “Rotationally cold OH^- ions in the cryogenic electrostatic ion-beam storage ring DESIREE”, *Phys. Rev. Lett.* **119**, 073001 (2017).
- ⁵³J. Arianer and R. Geller, “The advanced positive heavy ion sources”, *Annual Review of Nuclear and Particle Science* **31**, 19–51 (1981).
- ⁵⁴K. Nielsen, “The development of magnetic ion sources for an electromagnetic isotope separator”, *Nuclear Instruments* **1**, 289–301 (1957).
- ⁵⁵Source of negative ions by cesium sputtering (National Electrostatic Corporation, USA).
- ⁵⁶S. Rosén, H. T. Schmidt, P. Reinhed, D. Fischer, R. D. Thomas, H. Cederquist, L. Liljeby, L. Bagge, S. Leontein, and M. Blom, “Operating a triple stack microchannel plate-phosphor assembly for single particle counting in the 12–300k temperature range”, *Rev. Sci. Instrum.* **78**, 113301 (2007).
- ⁵⁷Z. Amitay and D. Zajfman, “A new type of multiparticle three-dimensional imaging detector with sub-nanosecond time resolution”, *Rev. Sci. Instrum.* **68**, 1387–1392 (1997).
- ⁵⁸A. F. Schmidt-May, “Final-state-resolved mutual neutralization of Li^+ and H^- ” (2022).
- ⁵⁹N. de Ruelle, A. Dochain, T. Launoy, R. F. Nascimento, M. Kaminska, M. H. Stockett, N. Vaeck, H. T. Schmidt, H. Cederquist, and X. Urbain, “Mutual neutralization of O^- with O^+ and N^+ at subthermal collision energies”, *Phys. Rev. Lett.* **121**, 083401 (2018).
- ⁶⁰M. Poline, A. Dochain, S. Rosén, J. Grumer, M. Ji, G. Eklund, A. Simonsson, P. Reinhed, M. Blom, N. S. Shuman, S. G. Ard, A. A. Viggiano, M. Larsson, H. Cederquist, H. T. Schmidt, H. Zettergren, X. Urbain, P. S. Barklem, and R. D. Thomas, “Mutual neutralisation of O^+ with O^- : investigation of the role of metastable ions in a combined experimental and theoretical study”, *Phys. Chem. Chem. Phys.* **23**, 24607–24616 (2021).
- ⁶¹Simion 3d version 6.0 user’s manual (1995).
- ⁶²G. Eklund, Experiments on mutual neutralization using storage rings with merged ion beams (Stockholm University, 2021).
- ⁶³R. E. Olson, “Absorbing-sphere model for calculating ion–ion recombination total cross sections”, *J. Chem. Phys.* **56**, 2979–2984 (1972).
- ⁶⁴B. F. Physics of ion-ion and electron-ion collisions, eng, Nato advanced study institute series Physics (Plenum Press, New York London, 1983).
- ⁶⁵U. Müller and P. C. Cosby, “Three-body decay of the $3s^2A'_1(N=1, K=0)$ and $3d^2E''(N=1, G=0, R=1)$ rydberg states of the triatomic hydrogen molecule H_3 ”, *Phys. Rev. A* **59**, 3632–3642 (1999).
- ⁶⁶D. Zajfman, Z. Amitay, C. Broude, P. Forck, B. Seidel, M. Grieser, D. Habs, D. Schwalm, and A. Wolf, “Measurement of branching ratios for the dissociative recombination of cold HD^+ using fragment imaging”, *Phys. Rev. Lett.* **75**, 814–817 (1995).
- ⁶⁷R. Dalitz, “CXII. on the analysis of τ -meson data and the nature of the τ -meson”, *The London, Edinburgh, and Dublin Philosophical Magazine and Journal of Science* **44**, 1068–1080 (1953).
- ⁶⁸A. Salop and R. E. Olson, “Charge exchange between $H(1s)$ and fully stripped heavy ions at low-keV impact energies”, *Phys. Rev. A* **13**, 1312–1320 (1976).
- ⁶⁹R. K. Janev and A. R. Tancic, “Recombination of h^+ and h^- ions in slow collisions”, *Journal of Physics B: Atomic and Molecular Physics* **5**, L250–L252 (1972).
- ⁷⁰C. Herring, “Critique of the Heitler-London method of calculating spin couplings at large distances”, *Rev. Mod. Phys.* **34**, 631–645 (1962).

- ⁷¹X. Zhou and A. Dickinson, “Mutual neutralisation of N^+ by O^- and O^+ by O^- in slow collisions”, *Nucl. Instrum. Methods B* **124**, 5–11 (1997).
- ⁷²E. Wigner and E. E. Witmer, “Über die struktur der zweiatomigen molekülspektren nach der quantenmechanik”, *Zeitschrift für Physik* **51**, 859–886 (1928).
- ⁷³C. Froese Fischer, G. Tachiev, G. Gaigalas, and M. R. Godefroid, “An MCHF atomic-structure package for large-scale calculations”, *Comput. Phys. Commun.* **176**, 559–579 (2007).
- ⁷⁴F. Jensen, *Introduction to computational chemistry* (Wiley, 2007).
- ⁷⁵R. E. Olson, J. R. Peterson, and J. Moseley, “Ion–ion recombination total cross sections—atomic species”, *J. Chem. Phys.* **53**, 3391–3397 (1970).
- ⁷⁶B. Peart, S. J. Foster, and K. Dolder, “Measurements of the mutual neutralisation of N^+/O^- and O^+O^- ”, *J. Phys. B: At. Mol. Opt. Phys.* **22**, 1035–1042 (1989).
- ⁷⁷D. A. Hayton and B. Peart, “Merged beam measurements of the mutual neutralization of O^+O^- and N^+/O^- ions”, *J. Phys. B: At. Mol. Opt. Phys.* **26**, 2879–2885 (1993).
- ⁷⁸*Ionization potentials of atoms and atomic ions* (1992), pp. 10–211.
- ⁷⁹S. J. Cavanagh, S. T. Gibson, M. N. Gale, C. J. Dedman, E. H. Roberts, and B. R. Lewis, “High-resolution velocity-map-imaging photoelectron spectroscopy of the O^- photodetachment fine-structure transitions”, *Phys. Rev. A* **76**, 052708 (2007).
- ⁸⁰A. Dochain, “Systematic study of mutual neutralization reactions between atomic species using the merged beam method and an asymptotic model” (2022).
- ⁸¹C. Froese Fischer and G. Tachiev, “Breit–pauli energy levels, lifetimes, and transition probabilities for the beryllium-like to neon-like sequences”, *Atomic Data and Nuclear Data Tables* **87**, 1–184 (2004).
- ⁸²S. M. MacDonald, J. C. Gómez Martín, R. Chance, S. Warriner, A. Saiz-Lopez, L. J. Carpenter, and J. M. C. Plane, “A laboratory characterisation of inorganic iodine emissions from the sea surface: dependence on oceanic variables and parameterisation for global modelling”, *Atmospheric Chemistry and Physics* **14**, 5841–5852 (2014).
- ⁸³T. H. Y. Yeung, “Recombination coefficients for positive and negative ions”, *Proceedings of the Physical Society* **71**, 341–346 (1958).
- ⁸⁴C. Greaves, “Ion-ion recombination in iodine afterglows”, *Journal of Electronics and Control* **17**, 171–180 (1964).
- ⁸⁵R. Peverall, S. Rosén, J. R. Peterson, M. Larsson, A. Al-Khalili, L. Vikor, J. Semaniak, R. Bobbenkamp, A. Le Padellec, A. N. Maurellis, and W. J. van der Zande, “Dissociative recombination and excitation of O_2^+ : cross sections, product yields and implications for studies of ionospheric airglows”, *J. Chem. Phys.* **114**, 6679–6689 (2001).
- ⁸⁶V. Zhaunerchyk, W. D. Geppert, M. Larsson, R. D. Thomas, E. Bahati, M. E. Bannister, M. R. Fogle, C. R. Vane, and F. Österdahl, “Three-body breakup in the dissociative recombination of the covalent triatomic molecular ion O_3^+ ”, *Phys. Rev. Lett.* **98**, 223201 (2007).
- ⁸⁷A. Petrigiani, F. Hellberg, R. D. Thomas, M. Larsson, P. C. Cosby, and W. J. van der Zande, “Vibrational dependence in the dissociative recombination of O_2^+ ”, *Journal of Physics: Conference Series* **4**, 182–186 (2005).